Surveys in Geophysics manuscript No.
(will be inserted by the editor)

Artifacts in high-frequency surface wave dispersion imaging

– Towards the linear receiver array

Feng Cheng · Jianghai Xia

Received: Jan, 2021 / Accepted: XX, XXXX

Abstract Surface wave methods are non-invasive, low-cost, and robust approaches to image near-surface S-wave velocity (Vs) structure. In terms of the energy source types, they can be classified in two groups: active-source surface wave methods and passive-source surface wave methods. A clean and high-resolution dispersion image is critical for the subsequent dispersion curve picking as well as Vs inversion for either the active-source surface wave methods or the passive-source surface wave methods. However, aliasing or other artifacts are almost inevitable in surface wave dispersion measurements in practice, and they can seriously pollute the measured dispersion spectra. It is significant to figure out how they are generated, how they affect the dispersion measurement, and how they can be attenuated. We provide the first comprehensive review on artifacts that are frequently observed in surface wave dispersion measurements, and summary them into three general types, including artifacts from spare spatial sampling, artifacts from array response, and artifacts from weak coherent signals. Both numerical and field examples, as well as mathematic derivations, are presented to help reader understand the generations of the various types artifacts and the way to attenuate them. This work will help us understand the complex components on the measured surface wave dispersion spectra, and lead to potential improvements on dispersion measurements.

Keywords Surface wave · Passive-source · Active-source · Dispersion measurement · Aliasing · Artifacts

F. Cheng
[1]Dept. of Earth, Environmental, and Planetary Sciences
Rice University
6100 Main St., Houston, TX 77005, USA
[2]Lawrence Berkeley National Laboratory
1 Cyclotron Rd., Berkeley, CA, 94720, USA
E-mail: marscfeng@rice.edu

J. Xia
School of Earth Sciences
Zhejiang University
38 Zheda Rd., Hangzhou, Zhejiang 310027, China
E-mail: jhxia@zju.edu.cn

1 Introduction

Surface waves are guided and dispersive. Shear (S)-wave velocity structure can be determined by inverting the dispersive phase velocity of surface waves (Dorman and Ewing, 1962), due to the higher sensitivity of dispersion curve to S-wave velocity than other earth properties, like compressional (P)-wave velocity, bulk density, and thickness, for a layered earth model (Xia et al., 1999). Surface wave methods, particularly techniques based on analysis of Rayleigh wave dispersion, have been widely utilized at multiple scales in engineering as well as classical geological studies (Miller et al., 1999; Xia et al., 1999, 2009; Socco et al., 2010; Nakata et al., 2011; Foti et al., 2018) with advantages in terms of both cost, acquisition time, and robustness in a variety of contexts. They can be classified in two groups associated with the energy source type: active-source surface wave methods and passive-source surface wave methods.

Active-source surface wave methods use hammers (Park et al., 1999), weight drops (Xia et al., 2000), or vibrators (Miller et al., 1999) as seismic sources. Stokoe and Nazarian (1983) and Nazarian et al. (1983) present the SASW method (spectral analysis of surface waves), which analyzes the dispersion curve of Rayleigh waves to produce near-surface S-wave velocity profiles. To improve inherent difficulties in evaluating and distinguishing signal from noise with only a pair of receivers in SASW measurements, the multichannel analysis of surface wave (MASW) method, typically using multiple geophones (i.e., 12–24), was developed (Song et al., 1989; Miller et al., 1999; Park et al., 1999; Xia et al., 1999, 2003, 2009; Socco et al., 2010; Park and Carnevale, 2010; Pan et al., 2019). With the development of horizontal excitation source as well as the multiple component instruments, multichannel analysis of Love wave (MALW) also draws more and more attentions (Song et al., 1989; Winsborrow et al., 2003; Safani et al., 2005; Zeng et al., 2007; Eslick et al., 2008; Xia et al., 2012; Yin et al., 2014; Pan et al., 2016a; Mi et al., 2018, 2020). A key step in the MASW, as well as MALW, is to generate reliable and high-resolution dispersion spectra; accurate dispersion curves can then be manually or automatically picked by following peaks of dispersion spectra along different frequencies and finally inverted for 1D Vs profiles. Several techniques are available for surface wave dispersion spectra calculation: the $\tau - p$ transformation (McMechan and Yedlin, 1981), the $f - k$ transformation (Yilmaz, 1987, p.430), the phase-shift method (Park et al., 1998), the frequency decomposition and slant stacking method (Xia et al., 2007), and the high-resolution linear Radon transformation (HLRT, Luo et al., 2008). Love wave dispersion measurements are usually simpler and cleaner than Rayleigh wave because Love waves are independent of P wave velocity.

The passive-source surface wave methods use ambient seismic energy from natural or anthropogenic sources (e.g., small earthquakes (Poupinet et al., 1984), ocean-seafloor interaction (Lepore and Grad, 2020), traffic (Nakata et al., 2011), industrial activities (Pan et al., 2016b)). During the past two decades, passive-source surface wave methods have gained booming development from the geophysical and civil engineering communities because of the logistical challenge and cost from traditional seismic surveys in highly populated urban areas. In fact, the first passive-source surface wave study originates over 60 years ago in pioneering works by Aki (1957, 1965), which is known as spatial autocorrelation (SPAC) method. Okada and Suto (2003) provided a comprehensive review of the SPAC method and further extended the SPAC method using microtremor array measurement (MAM) to improve the flexibility of the receiver configuration and the investigation depth of the objective structure. Aki's work has been revisited in light of advances of ambient noise interferometry technique following the groundbreaking work of Campillo and Paul (2003). Ambient noise interferometry is known for estimation Green's function between two receivers from the ambient seismic field (Shapiro and Campillo, 2004; Snieder, 2004; Wapenaar, 2004; Bensen et al., 2007; Snieder et al., 2009; Nakata et al., 2015). This approach has been applied to characterize multiple scales of earth structure: from global scale or continental scale deep-structure imaging in seismology (e.g., Yang et al., 2007; Lin et al., 2008; Yao and van der Hilst, 2009; Lin et al., 2009; Strobbia and Cassiani, 2011) to local scale exploration (e.g., Bakulin and Calvert, 2006; Wapenaar et al., 2008; Draganov et al., 2009; Nakata et al., 2011; Ali et al., 2013; Behm et al., 2014; Nakata et al., 2016; Castellanos et al., 2020).

Over the last decade, ambient noise interferometry has also found a variety of applications in the near-surface characterization domain (e.g., Foti et al., 2011; O'Connell and Turner, 2011; Xu et al., 2013; Cheng et al., 2015; Foti et al., 2018; Dou et al., 2017; Cheng et al., 2018a). Since ambient noise interferometry technique turns the physical receivers into virtual sources, it offers the potential to apply active-source methods, e.g., the phase-shift method, to the retrieved surface waves (Le Feuvre et al., 2015). Cheng et al. (2016) provided a method by combining ambient noise interferometry and multichannel analysis of surface wave for passive-source surface wave dispersion imaging, called multichannel analysis of passive surface waves (MAPS). In fact, several approaches have already existed and been popular in the seismic engineering communities in early 2000s. Louie (2001) presented the refraction microtremor (ReMi) method as a fast and effective passive-source surface wave imaging method based on the $\tau - p$ transformation, or slant-stacking (Thorson and Claerbout, 1985). Park et al. (2004) introduced a similar strategy for dispersion imaging of passive-source surface waves using the phase-shift method, called passive multichannel analysis of surface wave (PMASW).

Based on the data processing schemes of the previously mentioned passive-source surface wave methods, they can be roughly divided into two groups: non-interferometric methods (e.g., ReMi and PMASW) and interferometric methods (e.g., MAPS and SPAC). Non-interferometric methods directly extract dispersion measurements from ambient seismic records (Louie, 2001; Park et al., 2004), while interferometric methods calculate interferograms before dispersion measurements is applied, where interferograms are either empirical Green's function (Cheng et al., 2016; Xu et al., 2017) or spatial autocorrelation coefficients, also known as spatially averaged coherency (Asten, 2006; Chávez-García et al., 2006). Severals studies have provided explicit relationships between Green's function (or cross-correlation functions) and spatial autocorrelation results (Asten, 2006; Nakahara, 2006; Tsai and Moschetti, 2010; Haney et al., 2012). Interferometric methods appear more reasonable for utilization in passive-source seismic surveys. Because they retrieve interpretable signals with a specified virtual source (e.g., Green's function or spatially averaged coherency) from ambient seismic records, the process of dispersion analysis is analogous to active-source surface wave analysis (e.g., MASW). Recent works have argued that interferometric methods have advantages over non-interferometric methods (Cheng et al., 2016; Xu et al., 2017). Cheng et al. (In reviewb) provided comprehensive comparisons between non-interferometric and interferometric passive-source surface wave imaging methods, and concluded that the interferometric methods have the superiority for more accurate dispersion imaging in terms of the linear acquisition system.

No matter for the active-source surface wave methods or the passive-source surface wave methods, a clean and high-resolution dispersion image without aliasing or artifacts is critical for the subsequent dispersion curve picking as well as Vs inversion. Compared with the active-source methods, the passive-source methods have the advantage of extending the depth of investigation due to the broader bandwidth from abundant passive sources, particularly at lower frequencies. Since the temporal and spatial distribution of ambient noise sources are unknown, meanwhile, the passive-source methods also suffer from incoherent noises, particularly at higher frequencies. Aliasing or artifacts are almost inevitable for either active-source or passive-source surface wave surveys, although the former can usually provide much better dispersion measurements. Several studies have attempted to improve surface wave dispersion measurements, for example, by enhancing dispersion imaging resolution (Luo et al., 2008; Mikesell et al., 2017), and by deblurring of surface wave dispersion spectra (Picozzi et al., 2010; Cheng et al., In reviewa), and by analyzing and filtering surface wave energy (Park et al., 2002; Ivanov et al., 2005), and by selective stacking noise segments for passive-source surface wave dispersion imaging (Cheng et al., 2018b, 2019; Pang et al., 2019). Only a few studies were devoted to investigate how the aliasing or artifacts are generated, and how to attenuate them. Turner (1990) presented the aliasing problems in the $\tau - p$ transform due to the insufficient spatial sampling. Cheng et al. (2018b) first discussed a kind of "crossed" artifacts for high-frequency passive-source surface wave surveys, explained the underlying physics and proposed an effective way to attenuate them by using FK-based data selection. Dai et al. (2018) discussed the effects due to aliasing on wavefield decomposition.

In this work, we seek to provide a comprehensive review on artifacts that are frequently observed in surface wave dispersion measurements, and explore how they generate and how to eliminate them. The current paper is organized as follows. We first review the existing surface wave methods, including both active-source and passive-source methods, from the data processing workflow to the mathematic derivations of dispersion imaging scheme. Next, we summary three types of artifacts in surface wave dispersion measurements, including artifacts from spare spatial sampling, artifacts from array response, and artifacts from weak coherent signals. Both numerical examples and field examples, as well as mathematic derivations, are presented to help reader understand the generations of these different types artifacts and the way to attenuate them. We also make further discuss on artifacts from the non-interferometric methods and the directional noise sources, which directly affect the real dispersion energy and produce biased dispersion informations. Finally, we present a brief conclusions, as well as some recommendations, for surface wave dispersion imaging.

In this paper, we use terminology 'high-frequency surface wave' to limit the scope of this work to near surface scale including most of passive-source surface wave surveys with frequency band above 1Hz as well as active-source surface wave surveys with frequency band usually above 10Hz. The frequency band ($>$ 1Hz) is relative higher compared to the long period ($>$ 30s) for teleseismic surface waves used in global scale ambient noise applications. We focus on high-frequency ($>$

1Hz) surface waves because they contribute significantly to urban seismic noise in a broad frequency range from 1Hz to more than 45 Hz with maximum amplitudes between 1 and 10 Hz (Groos and Ritter, 2009). Besides, it is worth noting that this work focuses on the linear receiver array, which is often deployed for both passive-source and active-source surface wave investigations because of its high efficiency and convenience. In populated urban areas, it is challenging to construct dense 2-D arrays due to the spatial restrictions imposed by existing infrastructures. Linear receiver arrays are a natural geometry for road-side investigations utilizing receivers deployed on shoulders or median strip areas. Linear array techniques are also useful when processing distributed acoustic sensing (DAS) datasets, a recently developed technique which utilizes subsurface fiber-optic cables to capture earth vibrations for seismic imaging (Dou et al., 2017; Ajo-Franklin et al., 2019; Zhan, 2019).

2 Surface wave methods

Figure.1 provides a general flowchart for both the active-source surface wave methods and the passive-source surface wave methods. In order to explore the underlying physics of the potential aliasing as well as artifacts, we briefly review the workflow for both the active-source surface wave methods (e.g., MASW) and the passive-source surface methods (e.g., MAPS), and introduce the mathematic background for the corresponding dispersion measurement technique.

2.1 Active-source surface wave methods

The MASW method utilizes a multichannel recording system to estimate near-surface S-wave velocity from high-frequency Rayleigh waves. It usually consists of four steps: (a) acquisition of wide-band, high-frequency ground roll using a multichannel recording system (e.g., Song et al., 1989); (2) creation of linear algorithms to transform the time-offset $(x-t)$ domain wavefield into frequency-velocity $(f-v)$ or frequency-wavenumber $(f-k)$ domain dispersion spectra (e.g., Yilmaz, 1987; McMechan and Yedlin, 1981; Park et al., 1998; Xia et al., 2007; Luo et al., 2008); (3) extraction of accurate 1D dispersion curves manually or automatically (e.g., Dai et al., 2020; Ren et al., 2020); (4) development of stable and efficient inversion algorithms to obtain S-wave velocity profiles (e.g., Xia et al., 1999; Wathelet et al., 2004; Maraschini et al., 2010).

Dispersion measurement (imaging) is the vital step for surface wave methods. Slant-stacking algorithm has been primarily used as an array-based data processing method to extract phase velocity dispersion information from Rayleigh (e.g., Xia et al., 2009) and Love wave (e.g., Xia et al., 2012) for land seismic survey and Scholte wave for marine seismic survey (e.g., Bohlen et al., 2004). The phase-shift method (Park et al., 1998) is a typical presentation of frequency-domain slant-stacking method, which is popular for its efficiency and accuracy. Considering the similarity between different algorithms (e.g., Yilmaz, 1987; McMechan and Yedlin, 1981; Park et al., 1998; Xia et al., 2007; Luo et al., 2008), we focus on the phase-shift method to introduce the mathematic background. It will lead us to explore the underlying physics for the generation of the potential aliasing or artifacts.

Considering the offset-time $(x - t)$ domain representation $u(x,t)$ of a shot gather, the Fourier transform can be applied to time axis to obtain the frequency-offset $(f - x)$ domain wavefield $U(f,x)$,

$$U(f,x) = \int u(x,t)e^{i2\pi ft}dt, \tag{1}$$

where, the i denotes the imaginary unit. To obtain the frequency-velocity $(f - v)$ domain dispersion spectra, the phase-shift method applies the slant-stacking algorithm on the phase term of $U(f,x)$, or the whitened $f - x$ domain wavefield,

$$E(f,v) = \left| \sum_{j=1}^{N} e^{i2\pi f x_j/v} \frac{U(f,x_j)}{|U(f,x_j)|} \right|, \tag{2}$$

where, $E(f,v)$ is the measured dispersion spectra; x_j denotes the offset, $j \in (1..N)$. $e^{i2\pi f x_j/v}$ denotes the phase-shift term associated with the scanning velocity v at frequency f.

Following Aki and Richards (2002), a typical harmonic plane wave $U(f,x)$ can be expressed as

$$U(f,x) = A(f,x)e^{i(\phi_0 - 2\pi k_0 x)}, \tag{3}$$

where, ϕ_0 is the initial phase term; k_0 is wavenumber which is associated with the theoretical dispersion curve by $k = f/v$. Thus, we can simplify eq.2 by replacing $U(f,x)$ with eq.3,

$$\begin{aligned} E(f,k) &= \left| \sum_{j=1}^{N} e^{i2\pi k x_j} \frac{A(f,x_j)e^{i(\phi_0 - 2\pi k_0 x_j)}}{|A(f,x_j)e^{i(\phi_0 - 2\pi k_0 x_j)}|} \right| \\ &= |\sum_{j=1}^{N} e^{i\phi_0} e^{i(2\pi k - 2\pi k_0)x_j}| \\ &\approxeq |\sum_{j=1}^{N} e^{i2\pi(k-k_0)x_j}|. \end{aligned} \tag{4}$$

The energy peaks of $E(f,k)$ will be observed where k is approaching to the accurate dispersion curve k_0 of the coherent signal.

2.2 Passive-source surface wave methods

Figure.1 also presents the basic data processing schemes for two groups passive-source surface wave methods: the non-interferometric methods, for example, ReMi (Louie, 2001) and PMASW (Park et al., 2004), and the interferometric methods for example, MAPS (Cheng et al., 2016) and SPAC (Chávez-García et al., 2006). The key difference between the active-source and passive-source surface methods is that the later requires sufficient temporal and/or spectral ensemble averaging/stacking to enhance the coherent signals as well as cancel the incoherent signals from the inhomogeneous noise source distribution.

The data processing wokflow before dispersion picking and inversion is made up of four steps:
(1) Observation of the continuous and long-duration ambient noise records. In general, tens minutes duration is sufficient for urban passive-source surface wave survey.
(2) Splitting the continuous time series into short overlapped time segments. According to our experiences, a 20s window is good to ensure sufficient noise sources propagation range, as well as the efficiency of the ensemble averaging; too large a stack count will increase computing costs. We usually apply 75% overlap on each segment to increase the stack count.
(3) Preprocessing on the short time segment to remove potential near-field interferences and extend frequency bandwidth. The basic data preprocessing includes tapering two ends, removing the mean, linear trend, dead traces, as well as instrument response as necessary, temporal normalization, and spectral whitening, for each individual time segment.
(4) Dispersion spectra measurement which is different for the non-interferometric and interferometric method as indicated on Figure.1. As for the non-interferometric methods, e.g., PMASW and ReMi, active-source surface wave dispersion imaging algorithm will be directly applied on a series of preprocessed noise data; next the obtained dispersion spectra for each short time segment will be stacked to get the final improved dispersion spectra. As for the interferometric methods, e.g., MAPS and SPAC, cross-correlation or cross-coherence interferograms between each inter-station pair will be calculated and stacked along the time direction before the subsequent dispersion measurement.

Since the non-interferometric methods employ the same active-source dispersion imaging scheme as we previously described, we will not go through the derivation here. Severals studies have provided explicit relationships between Green's function (or cross-correlation functions) and spatial autocorrelation results (Asten, 2006; Nakahara, 2006; Tsai and Moschetti, 2010; Haney et al., 2012). For simplicity, we focus on the interferometric method, MAPS, to introduce the mathematic background for the dispersion imaging.

We follow the conventions in Cheng et al. (In reviewb) to present the cross-correlation spectrum C_{x_1,x_2} as

$$\begin{aligned} C_{x_1,x_2} &= u(x_1,\omega)u^*(x_2,\omega) \\ &= \sum_{j=1}^{N_s}(e^{-i2\pi k_0 x_1}e^{i2\pi k_0 x_2}) + \overline{C_{x_1,x_2}}, \end{aligned} \tag{5}$$

where, $\overline{C_{x_1,x_2}}$ is the cross term; ω is the angle frequency; $u(x_1,\omega)$ and $u(x_2,\omega)$ indicate the ambient noise spectral wavefield following the representation $u(x,\omega) = \sum_{j=1}^{N_s} e^{i(\omega t_{s_i} - 2\pi k_0 r_{s_i} - 2\pi k_0 x)}$ (eq.14 in Cheng et al. (In reviewb)) for the in-line source distribution case.

Because noise sources are assumed to be uncorrelated in time and space, and the contribution of each source to the cross-correlation function could be determined independently (Tromp et al., 2010; Lawrence et al., 2013), the cross term $\overline{C_{x_1,x_2}}$ is negligible with a sufficiently time-averaged ensemble. Applying the ensemble averaging along the time direction yields the cross-correlation spectrum here $\langle C_{x_1,x_2}\rangle$ under the in-line source distribution

$$\begin{aligned}\langle C_{x_1,x_2}\rangle &= \langle\sum_{j=1}^{N_s}(e^{-i2\pi k_0 x_1}e^{i2\pi k_0 x_2}) + \overline{C_{x_1,x_2}}\rangle \\ &\approxeq e^{-i2\pi k_0 x_{1,2}},\end{aligned} \tag{6}$$

where, $\langle ... \rangle$ indicates the ensemble averaging. We employ the slant-stacking algorithm by replacing the wavefield $U(f,x)$ in eq.2 with ensemble averaged cross-correlation spectrum $\langle C_{x_1,x_2}\rangle$ to obtain the MAPS representation

$$\begin{aligned}E(f,k) &= |\sum_{m=1}^{N-1}\sum_{n=m+1}^{N} e^{i2\pi k x_{m,n}}\frac{\langle C_{x_m,x_n}\rangle}{|\langle C_{x_m,x_n}\rangle|}| \\ &= |\sum_{m=1}^{N-1}\sum_{n=m+1}^{N} e^{i2\pi (k-k_0) x_{m,n}}|,\end{aligned} \tag{7}$$

where, $\sum_{m=1}^{N-1}\sum_{n=m+1}^{N}$ denotes the C_N^2 inter-station cross-correlation pairs. The energy peaks of $E(f,k)$ will be observed where k is approaching to the accurate dispersion curve k_0 of the coherent signal. Eq.7 demonstrates the ability of the interferometric method to produce the accurate dispersion curve. Reader is referred to Cheng et al. (In reviewb) for more details about the derivation for passive-source surface wave dispersion imaging, including the approximation and bias for the non-interferometric methods.

3 Artifacts in surface wave dispersion imaging

It is well-known that the active-source surface wave surveys usually provides much better and cleaner dispersion spectra than the passive-source surveys. In practice, however, aliasing or artifacts are almost inevitable for either active-source or passive-source surface wave surveys. We summary three types of artifacts that are frequently observed in surface wave dispersion spectra, and explore the underlying physics for the generation of these artifacts, as well as the solution to eliminate or attenuate them.

Note that as a review work, all field examples included in this work have already been reported before for various purposes. Most of the details about data collection and basic data processing have been omitted to force on the discussion about artifacts. Reader is invited to the corresponding reference for more details. Part of the measurements in this work might be different from the initial reports because of the difference on some specific data processing. For clearer presentation, all dispersion images in this work, except for Figure.10, have been normalized along the frequency direction.

3.1 Artifacts from spare spatial sampling

Spatial aliasing is a kind of artifacts due to undersampling or poor reconstruction. Therefore, it is usually related to the high frequencies. Several studies have been carried out to understand the aliasing (Turner, 1990; Li et al., 1991; Rafaely et al., 2007; Yan et al., 2016; Dai et al., 2018). In this work, we present a unique prospective on the generation of spatial aliasing in surface wave dispersion imaging.

Based on the derivations for the surface wave dispersion measurement (eq.4 and eq.7), we will observe the energy peaks of $E(f,k)$ when the scanning wavenumber $k = f/v$ for the phase-shift method is approaching to the accurate dispersion curve k_0 of the coherent signal. Due to the similarity between eq.4 and eq.7, we focus on the later to explore the underlying physics of the generation of spatial aliasing. Besides, the spatial aliasing is not a common issue for the active-source surface wave surveys due to their dense sampling acquisitions.

Given the evenly sampled acquisition system, which is commonly used in near-surface surface wave survey, we define $x_{m,n} = (m-n) * dx$ for simplicity, where dx denotes the spatial interval. We modify eq.7 using Euler formula as

$$
\begin{aligned}
E(f,k) &= |\sum_{m=1}^{N-1}\sum_{n=m+1}^{N} e^{i2\pi(k-k_0)x_{m,n}}| \\
&= |\sum_{m=1}^{N-1}\sum_{n=m+1}^{N} cos\{2\pi(k-k_0)x_{m,n}\} + i * sin\{2\pi(k-k_0)x_{m,n}\}| \\
&= |\sum_{m=1}^{N-1}\sum_{n=m+1}^{N} cos\{2\pi(m-n)(k-k_0)dx\} + i * sin\{2\pi(m-n)(k-k_0)dx\}|.
\end{aligned}
\tag{8}
$$

According to the periodicity of trigonometric function, k_0 is not the unique solution for eq.8. We list four potential solutions beyond k_0 as follows:

$$k = k_0 - \frac{j}{dx}, \ (k_0 > 0) \tag{9a}$$

$$k = k_0 + \frac{j}{dx}, \ (k_0 > 0) \tag{9b}$$

$$k = -k_0 + \frac{j}{dx}, \ (k_0 < 0) \tag{9c}$$

$$k = \frac{j}{dx}, \ (k_0 \ll dx) \tag{9d}$$

where, j denotes an non-negative integer value. Given a sufficient large dx, the aliasing k in eq.9 would posses high possibility to be located at the target window approaching k_0. Eq.9 presents the underlying physics for four types of aliasing energy that could be observed on surface wave dispersion spectra, particularly with the spare geometries. Figure.2 presents an example of four types of aliasing in $f-v$ domain with different spatial sampling intervals, $dx = 2m$ (a) and $dx = 10m$ (b). The black curve shows the theoretical dispersion curve calculated from a four-layer earth model (Tab.1) by Knopoff's method (Schwab and Knopoff, 1972). We predict four types of spatial aliasing based on eq.9 with $j = 1, 2, 3$. Four different colored curves, red, blue, cyan, green, indicate four different types of spatial aliasing, respectively. Figure.2 clearly illustrates the different characteristics for different types of spatial aliasing. It also explains one fact that spatial aliasing absolutely exists but will only be observed in relatively spare geometries since our interested windows on $f - v$ domain are limited. We further introduce three typical field examples to help reader understand these different types of spatial aliasing.

3.1.1 Spatial aliasing artifacts: type A and type B

According to eq.9a and 9b, the type A spatial aliasing has the less possibility to be observed on the low velocity surface wave target window compared to type B, because of the smaller wavenumber value which indicates the higher velocity value for a specific frequency. It is seldom to observe both types of spatial aliasing on the same surface wave dispersion image (Foti et al., 2018), although we can frequently observe type B spatial aliasing on surface wave dispersion spectra images. Here we present a typical example which was first reported by Hu et al. (2016). Figure.3a shows a 145-channel common-shot-point (CSP) gather with 10m spatial interval and 29.5m nearest offset, and both surface waves (ground-roll wave) and body waves are visible. Figure.3b displays the dispersion spectra obtained by using the phase-shift method. The multi-mode surface waves energy with low velocity ($<$ 0.5km/s) and low frequency ($<$ 10Hz) can be observed on the bottom left of Figure.3b. However, the dispersion spectra is dominated by the non-dispersive body waves, which are represented by the strong horizontal dispersion energy belts around 1.8km/s (the blue dotted line). Weak air waves energy is also visible at velocity around 0.34km/s as indicated by the red dotted line. Based on eq.9, we are able to predict any type of spatial aliasing for all observed wave types by replacing the objective dispersion curve k_0 with the picked dispersion energy peaks of surface waves, body waves, and air waves. We find the type A spatial aliasing from air wave and the type B spatial aliasing from the body wave are located inside the spectra window, and match well with the artifacts energy at the top right (the red diamond curves) and at the bottom right (the blue dash-dot curves) of Figure.3b, respectively. Although the spatial aliasing from the surface waves are not observed on the objective spectra range, the good match between the predicted aliasing and the observed artifacts convince us the derivation on the spatial aliasing (eq.9).

3.1.2 Spatial aliasing artifacts: type C

According to eq.9c, the type C spatial aliasing will be generated when $k_0 < 0$. It indicates the slant-stacking algorithm is scanning a reverse propagating surface wave instead of the normal forward propagating one ($k_0 > 0$). In fact, eq.9c is consistent with the finding by Cheng et al. (2018b), which firstly demonstrated the existence of a type of "crossed" aliasing due to the bidirectional velocity scanning in the dispersion analysis. It usually happens to the non-interferometric passive-source surface wave methods, because they include both the forward and the reverse velocity during the slant-stacking scanning procedure, and sum the dispersion spectra from both directions in order to account for the possible bidirectional nature of the recorded passive-source surface waves. In general, the summation operator in the non-interferometric methods is reasonable and safe because the propagation direction of the incoming surface wave is unclear. However, this ambiguity produces the “crossed” aliasing in dispersion measurement, which is exactly the type C spatial aliasing discussed in this work, and the “crossed” aliasing could seriously smear the dispersion energy, particularly at the higher frequency band and the higher oder components.

We present an example of the type C spatial aliasing on Figure.4 from 10-min traffic noise records with a 24 vertical-component receiver array. The spatial interval is 10m. The same dataset has been first reported by Cheng et al. (2018b). Based on eq.9c, we predict the spatial aliasing using the picked multi-mode dispersion curves from each dispersion measurement, separately. The predicated type C spatial aliasing generally matches with the "crossed" artifacts (Figs. 4a, b and c), although distortions exist due to errors from dispersion curve picking.

We observe only MAPS method produces the clean dispersion spectra (Fig.4d) because the direction of the scanning velocity can be defined by the retrieved empirical Green's function or interferograms. Besides, Cheng et al. (2018b) provided an effective technique with FK-based data-selection to attenuate this type of aliasing. Xi et al. (2020) proposed to use the Wiener filter based on singular value decomposition (SVD) to attenuate the "crossed" artifacts. The existence of weak "crossed" aliasing in the SPAC measurement (Fig.4c) is supposed to be directly related with the bidirectional characteristic of Bessel function or Hankel function (Forbriger, 2003), and can be attenuated by replacing the Bessel function used in SPAC with the adaptive Hankel functions (Xi et al., In Review).

3.1.3 Spatial aliasing artifacts: type D

According to eq.9d, the type D spatial aliasing is independent with the real dispersion energy, and possesses a series of constant wavenumber values. Therefore, it is much easier to be distinguished on surface wave dispersion spectra. On the contrary, the other three types of spatial aliasing are dependent with the real dispersion energy, and these aliasing energy will present the similar energy distribution along the frequency direction as the real dispersion energy.

Figure.5 shows an example of the type D spatial aliasing. The dataset consists of 16 days ambient noise data recorded by 35 broadband seismometers (Trillium 120 P/PA), which has been reported by Xu et al. (2016) and Pan et al. (2016b). The spatial interval is around 1km. We apply ambient noise interferometry to retrieve the coherent Rayleigh waves from the vertical component. We stack over all interstation pairs into discrete offset bins (Fig.5a) to further enhance the coherent signals. The bin size of the spatial stacking is of 1km. Figure.5b presents the obtained dispersion spectra using MAPS. The distinct linear artifacts can be easily distinguished as the type D spatial aliasing using the predicted aliasing (the green dashed line) from eq.9d.

Since the type D spatial aliasing presents as linear artifacts with constant wavenumber, it can be easily attenuated in $f-k$ domain using filter techniques, for example, the median filter and the FK filter. Figure.5c displays an example of aliasing attenuation using the FK filter. The dispersion spectra has been significantly improved with the extended frequency bandwidth and the attenuated distortions at low frequencies. However, some weak linear aliasing artifacts still exist at high frequency due to the leakage of the FK filter.

According to the Nyquist theorem, we can define the maximum wavenumber as the two times of the Nyquist wavenumber, $k_{max} = 2 * \frac{1}{2*dx} = \frac{1}{dx}$. k_{max} can be taken as an effective quality control factor for surface wave dispersion imaging, and provide a reference for the available maximum frequency boundary.

3.2 Artifacts from array response

Array geometry configuration is vital for seismic acquisitions. Eq.9 demonstrates the spatial aliasing is directly associated with the spatial sampling interval, which controls the maximum wavenumber observed with the array. It usually affects the ability of the array for high frequency seismic signals acquisition. Nevertheless, the ability for the minimum wavenumber is dominated by the length of the array with the relationship ($k_{min} = \frac{1}{Array\ length}$), which can be taken as the absolute wavenumber resolution according to the Fourier analysis. It indicates the maximum array length (L) affects the imaging resolution of the surface wave dispersion spectra.

Here we employ the array response function (ARF) concept to present the influence of the array geometry on dispersion measurement (Capon, 1969; Rost and Thomas, 2002; Picozzi et al., 2010; Liu et al., 2020). The array response function is also called the array smooth function (ASF) as the spectral estimator in some literatures (Johnson and Dudgeon, 1993; Boiero and Socco, 2011; Bergamo et al., 2012). We define the ARF as

$$ARF(k) = |\sum_{i=1}^{N} e^{j(k-k_0)x_i}|. \tag{10}$$

For comparison, two numerical tests with different array lengths, 50m (Fig.6a) and 250m (Fig.6b), are carried out to generate 15-min ambient noise records with the random distributed sources configuration. Reader is referred to Cheng et al. (2016) for more details about ambient noise modeling. Figure.7a presents the corresponding normalized ARFs for two arrays. We observe the ARF curve (the pink curve) of the shorter array posses the broader (lower kurtosis) main lobe and distinct side lobes. As for the slantstacking-based dispersion imaging methods, the main lobe of the ARF determines the imaging resolution. Figure.7b and Figure.7c present the obtained dispersion spectra using the MAPS method for two arrays. We overlay the dispersion spectra with the ARF curves. For a specific frequency, i.e. 17Hz on Figure.7b and Figure.7c, the main lobes of the ARFs match well with the dominant dispersion energy bandwidth, and the peaks of ARFs are consistent with the peaks of the accurate dispersion energy. In general, the shorter array produces lower resolution spectral imaging, and vice versa.

The weak wiggles around the dominant dispersion energy (as indicated by the black arrows on Fig.7b) coincide with the side lobes of the ARFs, and can be taken as artifacts from the array response. In practice, the array response artifacts on dispersion spectra might be misidentified as weak higher modes. Moreover, the wiggles could emphasize smearing from the incoherent noise on the dispersion spectra. Therefore, Cheng et al. (In reviewa) proposed a phase-weighted slant-stacking technique for surface wave dispersion measurement in order to enhance coherent signals as well as attenuate artifacts from array response on dispersion spectra.

k_{min} controls not only the imaging resolution but also the limitation of the bottom frequency for the dispersion measurement. Because the minimum wavenumber is linearly associated with the lowest frequency for most of the increasing velocity earth model. We carry out two similar numerical tests based on two arrays with different array lengths, 100m and 20m, to generate 15-min ambient noise records with the same random distributed source configuration as indicated on Figure.6. We apply the MAPS method on the generated noise records from two arrays to obtain dispersion spectra (Fig.8). Note that no data preprocessing operator is included prior to noise cross-correlation to avoid potential effects from the preprocessing operators, like spectra whitening, on the frequency bandwidth of the dispersion spectra. Figure.8 shows that the obtained dispersion spectra coincides with the accurate dispersion curve before the scanning wavenumber reaches k_{min} as indicated by the pink dashed line. The dispersion energy below k_{min} is biased from the accurate dispersion curve because the scanning wavenumber is beyond the absolution resolution of wavenumber (k_{min}).

Therefore, we can approximately regard k_{min} as a quality control indicator to avoid the artifacts. It is worth noticing that it is possible to enhance the apparent wavenumber resolution by increasing the sampling number of the Fourier transform, for example, padding zero-value traces (Cerna and Harvey, 2000). It indicates k_{min} is not a strict limitation, because the minimum scanning wavenumber in field application is possible to go beyond k_{min}. But k_{min} can still provide a soft reference for the available minimum frequency boundary.

3.3 Artifacts from weak coherent signals: the radial pattern artifacts

The frequency band of observed seismic record is finite, and usually dependent on the source spectrum distribution. In general, for the hammer activated surface waves, the observed frequency band is usually above 10Hz; for the traffic-induced surface waves in urban area, the observed frequency band is usually between 1Hz and 10Hz. If we force the mathematic algorithms to measure surface wave dispersion spectra beyond the recorded frequency band, artifacts will be produced. For example, if we give a very small value to $U(f, x)$, the computation of $U(f, x)/|U(f, x)|$ in eq.2 will be unstable. For the scanning frequencies beyond the acceptable frequency band, the measurement of eq.4 will be dominated by the term $e^{i2\pi kx}$, which is associated with the array response and is frequency independent. Thus, it will produce artifacts with constant wavenumber values which present as radial pattern energy on $f-v$ domain dispersion spectra. We call this type of artifacts as radial pattern artifacts. Besides, the type D spatial aliasing can also be taken as one special case of radial pattern artifacts.

Here, we present one active-source numerical example and two passive-source field examples to introduce the radial pattern artifacts, and, more importantly, discuss the influences from different data processing procedures on attenuation of this type of artifacts.

3.3.1 Numerical example

An active-source surface wave shot gather from a two-layer earth model (Table.2) was generated using a finite-difference solver, SOFI2D (Bohlen, 2002), with a 25Hz ricker wavelet and 30m nearest offset. Figure.9a shows the synthetic Rayleigh wave observed with a 60-channel linear receiver array with 1m spatial interval. Figure.9b displays the corresponding dispersion measurement obtained using the phase-shift method. We can observe distinct radial pattern energy at the high frequency ($>$ 65Hz) band as well noisy artifacts at the lower frequency ($<$ 5Hz) band. After spectral analysis, we find these artifacts at two ends are co-located with the weak spectrum energy, where the spectrum amplitudes are approaching to zero (Fig.9c).

In order to better display the characteristic of the radial pattern artifacts, we present the obtained dispersion spectra without frequency-direction normalization on both $f-k$ domain (the top panels on Fig.10) and $f-v$ domain (the bottom panels on Fig.10), respectively. Note that we break the frequency axis to emphasize the lower frequency band. On the $f-k$ domain dispersion spectra, a series of horizontal artifacts are located at two ends as indicated by the black arrows; on the $f-v$ domain dispersion spectra, a series of radial pattern artifacts are located at two ends as indicated by the black arrows. It coincides with our previous discussions that dispersion imaging beyond the recorded frequency band will produce radial pattern artifacts. Besides, we can also distinguish the consistency between the horizontal artifacts at lower frequency ($<$ 5Hz) and wiggles from the array response artifacts at the higher frequency ($>$ 6Hz). It indicates the connection between the array response and the radial pattern artifacts, and the possibility to attenuate the radial pattern artifacts by attenuating the array response artifacts as previously described.

3.3.2 Field example #1

Figure.11 presents a passive-source field example of the radial pattern artifacts. 5-min ambient noise data were recorded by a linear array of 38 Zland nodes (5 Hz) with 2ms sampling rate and 1m spatial-interval. The dataset has been first reported by Liu et al. (2020). Figure.11a shows the bin-stacked virtual source gather retrieved from ambient noise interferometry without noise data whitening preprocessing (Bensen et al., 2007). We apply the MAPS method for dispersion analysis. The obtained dispersion spectra presents two distinct radial pattern artifacts as highlighted by the black dashed line. We can also observe weak spatial aliasing at the right bottom. After including the whitening preprocessing procedure prior to the cross-correlation, however, we observe the mentioned two types of artifacts have been significantly eliminated on the obtained dispersion spectra (Fig.12a). It indicates the spectral whitening preprocessing is able to attenuate the strong radial pattern artifacts.

Ambient noise whitening is an important data preprocessing technique, which aims to balance the noise spectrum and extend the frequency bandwidth of the retrieved coherent signals from ambient noise cross-correlation. In order to figure out the influences of the spectral whitening on cross-correlation, we apply spectral analysis on the extracted cross-correlations. Two different colored curves on Figure.12b shows the normalized spectrum of the cross-correlations without whitening (the dark blue curve) and with whitening (the pink curve), respectively. We observe the distinct enhancement of the spectrum energy at lower frequency band ($<$ 5Hz) after whitening. Besides, the spectrum energy has been balanced between the frequencies below and above 15Hz. It indicates spectrum balance from the spectral whitening preprocessing makes contribution to the attenuation of the radial pattern artifacts.

According to Prieto et al. (2009), performing cross-correlation with spectral whitening is strictly equivalent to calculating the cross-coherence H_{x_1,x_2},

$$H_{x_1,x_2} = \frac{u(x_1,\omega)u^*(x_2,\omega)}{|u(x_1,\omega)||u(x_2,\omega)|}. \tag{11}$$

In some degree, it indicates the advantage of cross-coherence over cross-correlation in passive-source surface wave imaging (Nakata et al., 2011). However, pseudo arrivals generated by spectral whitening or cross-coherence with scattered waves should also be aware of, particularly for the low frequency targets (Nakata, 2020). It is worth noticing that some spikes on the spectrum (the pink curves) have been enhanced after whitening, and these spikes are associated with the spikes on the dispersion spectra around frequencies, 22Hz, 31Hz, 39Hz. The conventional spectral de-spiking processing (Girard and Shragge, 2019) seems to fail to remove these spikes on dispersion spectra, since the slant-stacking algorithm will emphasize them even after spectral de-spiking. Further studies are required to attenuate these spikes on dispersion spectra.

3.3.3 Field example #2

According to eq.7, MAPS includes the whole C_N^2 inter-station cross-correlation pairs for dispersion imaging. However, many passive-source surface wave applications using ambient noise cross-correlation only include one virtual-source gather (C_N^1) located at one end of the receiver array (Zhang et al., 2020; Li et al., 2020), because they still follow the conventional active-source surface wave, e.g., MASW, acquisition strategy. It means many useful informations will be wasted. On the other hand, the array responses for one virtual-source gather and multiple virtual-sources gather are also different. Figure.13 shows a comparison between ARFs for one virtual-source gather (C_N^1 inter-station pairs) and multiple virtual-sources gather (C_N^2 inter-station pairs). Here we take an array of 24 sensors with 10m spatial interval as example. The ARF of multiple virtual-sources gather (the black curve) shows smoother side lobes than that of one virtual-source gather (the red dashed curve). Compared with the wiggles of one virtual-source gather, the smoother side lobes decrease the possibility to be coupled with incoherent noise.

Here, we present an example to show the performances of the interferometric method, MAPS, on dispersion imaging with different virtual-source gathers. The dataset has been first reported by Cheng et al. (2019), which was collected along a busy railway over 30-min using a 24-channel linear array. The spatial interval is 10m. We first apply ambient noise interferometric to retrieve empirical Green's functions. Figure.14a presents the configuration of virtual source and virtual receiver for the multiple virtual-sources gather. Figure.14b displays the retrieved C_N^2 inter-station cross-correlation pairs. The yellow box highlights the one virtual-source gather with the first trace as the virtual source.

Figure.15 shows a comparison between the obtained dispersion spectra by using one virtual-source gather (Fig.15a) and the whole multiple virtual-sources gather (Fig.15b). With more data included, the dispersion spectra from the multiple virtual-sources gather is more continuous and much cleaner with less distortions and less radial pattern artifacts. Although spectral whitening is applied prior to cross-correlation for both dispersion measurements, radial pattern artifacts still exist on Figure.15a and Figure.15b as indicated by the black dashed lines. It indicates spectral whitening does not apply to all datasets for radial pattern artifacts attenuation. In fact, no one technique can do that.

Data-selection is an important technique for data quality control. Several studies have successfully applied data-selection on passive-source surface wave imaging (e.g., Cheng et al., 2018b; Zhou et al., 2018; Cheng et al., 2019; Pang et al., 2019). Here, we present an example of radial pattern artifacts attenuation (Fig.16) after applying automatic data selection in $\tau-p$ domain (Cheng et al., 2019). We observe the dispersion spectra has been much improved with the radial pattern artifacts significantly attenuated. Reader is referred to Cheng et al. (2019) for more details about the data selection technique.

4 Discussion

As the first review work on the artifacts in surface wave dispersion imaging, we admit that we might not be able to include all the existing artifacts but the presented three types of artifacts in this work are significant for understanding the complex components on the dispersion measurements and lay a foundation for the further work.

All previously mentioned artifacts, including spatial aliasing, array response artifacts, and radial pattern artifacts, present as the external energy, which usually exists around the accurate dispersion energy but could seriously smear the accurate dispersion peaks. However, there are also some artifacts that directly affect the real dispersion energy and produce biased dispersion informations. Here, we discuss two types of these artifacts: artifacts from the non-interferometric passive-source methods, and artifacts from the directional noise sources.

4.1 Artifacts from the non-interferometric passive-source methods

Cheng et al. (In reviewb) presents a comprehensive comparison between the non-interferometric methods and the interferometric methods. Numerical tests and field examples demonstrate that the non-interferometric methods cannot provide accurate dispersion measurement as the interferometric methods under the off-line distributed sources, e.g., away from the roadside. Compared with the accurate dispersion spectra that can be obtained from the interferometric methods, these biased dispersion energy measured by the non-interferometric methods can be taken as artifacts.

Here we present an example of the artifacts from the non-interferometric methods. The dataset is reported by Cheng et al. (In reviewb). A linear array of 48 RefTek 125A digitizers connected to 2.5 Hz vertical-component geophones was deployed along a busy road with an offset around 20∼30m from the survey line to the road. Figure.17 presents a comparison of the obtained dispersion spectra between the non-interferometric methods, PMASW (Fig.17a) and ReMi(Fig.17b), and the interferometric methods, SPAC (Fig.17c) and MAPS (Fig.17d). The black crosses indicate the picked dispersion curve based on the MAPS measurement. The shifts between the dispersion energy peaks from the non-interferometric dispersion measurements and the picked dispersion peaks indicate the biases produced by the non-interferometric methods. Therefore, Louie (2001) indicated that an interpreter must pick the lower edge of energy peaks of phase velocities on the ReMi measurements, rather than the dispersion energy peaks, and hypothesized that the off-line triggered sources caused the higher apparent velocities. However, this bias phenomenon is not unique to the ReMi method but is relevant to all linear-array-based non-interferometric passive-source surface wave methods. Cheng et al. (In reviewb) provided a way to estimate the biases in non-interferometric measurements by using the defined array smoothing function (ASF).

4.2 Artifacts from directional noise sources

It is well known that the empirical Green's function can be extracted by cross-correlating two receivers under the random distributed noise sources. In practice, the noise source distribution is rarely perfect random but inhomogeneous. Cheng et al. (2016) presented that the directional noise sources could produce biased cross-correlations, as well as dispersion measurements, particularly for linear receiver array. In order to attenuate the azimuthal effect on dispersion measurements, Cheng et al. (2016) proposed to apply azimuthal adjustment to the slant-stacking algorithm for accurate dispersion imaging. It still remains a realistic challenge for azimuth detection using the linear array. In order to obtain the accurate dispersion measurement based on the linear array, Liu et al. (2020) adapted the frequently used linear receiver array into the pseudo-linear array by adding two more off-line receivers to increase the array response to off-line signals.

We apply the 2D ARF concept to explain the limitation of linear array. For the consistency, we simply adapt the ARF on eq.10 from 1D to 2D as,

$$ARF(k,\theta) = |\sum_{j=1}^{N} e^{ik(x_j cos\theta + y_j sin\theta) - ik_0(x_j cos\theta_0 + y_j sin\theta_0)}|, \tag{12}$$

where, x_i and y_i indicates the receiver location in Cartesian coordinates. 2D ARF has the ability to illustrate the array response or beamforming resolution to a plane wave. Figure.18 presents a comparison of ARFs between the linear array (the left panel) and the pseudo-linear array (the right panel). We take a plane wave at frequency 15Hz and velocity 0.3km/s as example. We observe that the multiple beamer peaks for the linear array can not focalize to the target azimuth and velocity; while the adapted pseudo-linear array shows the high resolution response to the input plane wave with beamer energy peaks focalized at the accurate location (the pink circle). It indicates the linear array can not solve the 2D beamforming problems that simultaneously includes azimuth and velocity. Thus, Cheng et al. (2016) suggested to define an average velocity for azimuth detection. However, the pseudo-linear array geometry provides a solution in a clever way.

5 Conclusions

We summary three types of artifacts that are frequently observed in surface wave dispersion measurements, including the artifacts from spare spatial sampling, artifacts from the array response, and artifacts from weak coherent signals. We present how these artifacts are generated and how these artifacts can be attenuated. It will help us understand the complex components on obtained surface wave dispersion spectra, and lead to potential improvements on dispersion measurements. It also suggests us:

(1) the shorter spatial interval dx will extend the maximum wavenumber k_{max}, and usually leads to higher top frequency limitation that can be observed on dispersion spectra;

(2) the longer array length L will increase the dispersion imaging resolution with the smaller minimum wavenumber k_{min}, and usually leads to lower bottom frequency limitation that can be observed on dispersion spectra;

(3) the spectral whitening is critical to broaden frequency bandwidth for surface wave dispersion imaging, particularly for the passive-source surface wave imaging;

(4) the cross-coherence algorithm is recommended for the applications of the interferometric methods, since it has the advantage of including spectral whitening when cross-correlating;

(4) the multiple virtual-sources gather (C_N^2) is prior to the one virtual-source gather (C_N^1) for passive-source surface wave imaging, which will increase the data utilization and attenuate the array response artifacts.

Considering the limitation of the expensive instruments, the shorter spatial interval and the longer array length are always in conflict for the conventional nodal-based or cable-based seismic survey. We have to make a trade-off between the higher frequency limitation with the denser array and the lower frequency requirement with the longer array. However, recent advances in distributed acoustic sensing (DAS) acquisition provide routes to solve these problems; DAS in particular allows for acquisition over tens of kilometers while providing spatial sampling in the meter range, thus enabling local surface wave analysis with high fidelity (Ajo-Franklin et al., 2019).

Acknowledgements This study was supported by the National Natural Science Foundation of China under grant no. 41830103. We thank SISL team, as well as AoCheng Tech crews, for the field-data acquisitions. We would like to thank Changjiang Zhou, Chaoqiang Xi, Jingyin Pang, Tianyu Dai and Ya Liu for many useful discussions.

Conflict of interest

The authors declare that they have no conflict of interest.

References

Ajo-Franklin JB, Dou S, Lindsey NJ, Monga I, Tracy C, Robertson M, Rodriguez Tribaldos V, Ulrich C, Freifeld B, Daley T, Li X (2019) Distributed Acoustic Sensing Using Dark Fiber for Near-Surface Characterization and Broadband Seismic Event Detection. Scientific Reports 9(1):1328, DOI 10.1038/s41598-018-36675-8

Aki K (1957) Space and time spectra of stationary stochastic waves, with special reference to microtremors. Bulletin of the Earthquake Research Institute 35:415–456

Aki K (1965) A Note On The Use Of Microseisms In Determining The Shallow Structures Of The Earth's Crust. GEOPHYSICS 30(4):665–666, DOI 10.1190/1.1439640

Aki K, Richards PG (2002) Quantitative seismology. University Science Books

Ali MY, Barkat B, Berteussen KA, Small J (2013) A low-frequency passive seismic array experiment over an onshore oil field in Abu Dhabi , United Arab Emirates. Geophysics 78(4):B159–B176

Asten MW (2006) On bias and noise in passive seismic data from finite circular array data processed using SPAC methods. Geophysics 7(6):153–162

Bakulin A, Calvert R (2006) The virtual source method: Theory and case study. Geophysics 71(4):139–150

Behm M, Leahy GM, Snieder R (2014) Retrieval of local surface wave velocities from traffic noise - an example from the La Barge basin (Wyoming). Geophysical Prospecting 62(2):223–243

Bensen GD, Ritzwoller MH, Barmin MP, Levshin AL, Lin F, Moschetti MP, Shapiro NM, Yang Y (2007) Processing seismic ambient noise data to obtain reliable broad-band surface wave dispersion measurements. Geophysical Journal International 169:1239–1260

Bergamo P, Boiero D, Socco LV (2012) Retrieving 2D structures from surface-wave data by means of space-varying spatial windowing. Geophysics 77(4):EN39, DOI 10.1190/geo2012-0031.1

Bohlen T (2002) Parallel 3-d viscoelastic finite difference seismic modelling. Computers & Geosciences 28(8):887–899

Bohlen T, Kugler S, Klein G, Theilen F (2004) 1.5D inversion of lateral variation of Scholte-wave dispersion. Geophysics 69(2):330, DOI 10.1190/1.1707052

Boiero D, Socco LV (2011) The meaning of surface wave dispersion curves in weakly laterally varying structures. Near Surface Geophysics 9:561–570, DOI 10.3997/1873-0604.2011042

Campillo M, Paul A (2003) Long-range correlations in the diffuse seismic coda. Science 299(5606):547–549

Capon J (1969) High-Resolution Frequency-Wavenumber Spectrum Analysis. Proceedings of The IEEE 57(8):1408–1418

Castellanos JC, Clayton RW, Juarez A (2020) Using a Time-Based Subarray Method to Extract and Invert Noise-Derived Body Waves at Long Beach, California. Journal of Geophysical Research: Solid Earth 125(5), DOI 10.1029/2019JB018855

Cerna M, Harvey AF (2000) The fundamentals of fft-based signal analysis and measurement. Tech. rep., Application Note 041, National Instruments

Chávez-García FJ, Rodríguez M, Stephenson WR (2006) Subsoil structure using SPAC measurements along a line. Bulletin of the Seismological Society of America 96(2):729–736, DOI 10.1785/0120050141

Cheng F, Xia J, Xu Y, Xu Z, Pan Y (2015) A new passive seismic method based on seismic interferometry and multichannel analysis of surface waves. Journal of Applied Geophysics 117:126–135

Cheng F, Xia J, Luo Y, Xu Z, Wang L, Shen C, Liu R, Pan Y, Mi B, Hu Y (2016) Multi-channel analysis of passive surface waves based on cross-correlations. Geophysics 81(5):EN57–EN66

Cheng F, Xia J, Shen C, Hu Y, Xu Z, Mi B (2018a) Imposing active sources during high-frequency passive surface-wave measurement. Engineering 4(5):685–693

Cheng F, Xia J, Xu Z, Hu Y, Mi B (2018b) Frequency – Wavenumber (FK)-Based Data Selection in High - Frequency Passive Surface Wave Survey. Surveys in Geophysics 39:661–682

Cheng F, Xia J, Behm M, Hu Y, Pang J (2019) Automated Data Selection in the Tau–p Domain: Application to Passive Surface Wave Imaging. Surveys in Geophysics pp 1–18, DOI 10.1007/s10712-019-09530-2

Cheng F, Xia J, Kai Z, Changjiang Z, Ajo-Franklin J (In reviewa) Phase-weighted slant-stacking for surface wave dispersion measurement. Geophysical Journal International

Cheng F, Xia J, Xu Z, Ajo-Franklin J (In reviewb) Comparisons between non-interferometric and interferometric passive surface wave imaging methods - towards linear receiver array. Geophysical Journal International

Dai T, Hu Y, Ning L, Cheng F, Pang J (2018) Effects due to aliasing on surface-wave extraction and suppression in frequency-velocity domain. Journal of Applied Geophysics 158:71–81, DOI 10.1016/j.jappgeo.2018.07.011

Dai T, Xia J, Ning L, Xi C, Liu Y, Xing H (2020) Deep Learning for Extracting Dispersion Curves. Surveys in Geophysics (August), DOI 10.1007/s10712-020-09615-3

Dorman J, Ewing M (1962) Numerical inversion of seismic surface wave dispersion data and crust-mantle structure in the new york-pennsylvania area. Journal of Geophysical Research 67(13):5227–5241

Dou S, Lindsey N, Wagner AM, Daley TM, Freifeld B, Robertson M, Peterson J, Ulrich C, Martin ER, Ajo-Franklin JB (2017) Distributed Acoustic Sensing for Seismic Monitoring of The Near Surface: A Traffic-Noise Interferometry Case Study. Scientific Reports 7(1):11620, DOI 10.1038/s41598-017-11986-4

Draganov D, Campman X, Thorbecke J, Verdel A, Wapenaar K (2009) Reflection images from ambient seismic noise. Geophysics 74(5):A63–A67

Eslick R, Tsoflias G, Steeples D (2008) Field investigation of love waves in near-surface seismology. Geophysics 73(3):G1–G6

Forbriger T (2003) Inversion of shallow-seismic wavefields: I. Wavefield transformation. Geophysical Journal International 153(3):719–734, DOI 10.1046/j.1365-246X.2003.01929.x

Foti S, Parolai S, Albarello D, Picozzi M (2011) Application of surface-wave methods for seismic site characterization. Surveys in geophysics 32(6):777–825

Foti S, Hollender F, Garofalo F, Albarello D, Asten M, Bard PY, Comina C, Cornou C, Cox B, Di Giulio G, et al. (2018) Guidelines for the good practice of surface wave analysis: A product of the interpacific project. Bulletin of Earthquake Engineering 16(6):2367–2420

Girard AJ, Shragge J (2019) Automated processing strategies for ambient seismic data. Geophysical Prospecting pp 1–20, DOI 10.1111/1365-2478.12794

Groos JC, Ritter JRR (2009) Time domain classification and quantification of seismic noise in an urban environment. Geophysical Journal International 179(2):1213–1231, DOI 10.1111/j.1365-246X.2009.04343.x

Haney MM, Mikesell TD, van Wijk K, Nakahara H (2012) Extension of the spatial autocorrelation (spac) method to mixed-component correlations of surface waves. Geophysical Journal International 191(1):189–206

Hu Y, Wang L, Cheng F, Luo Y, Shen C, Mi B (2016) Ground-roll noise extraction and suppression using high-resolution linear Radon transform. Journal of Applied Geophysics 128:8–17, DOI 10.1016/j.jappgeo.2016.03.007

Ivanov J, Park CB, Miller RD, Xia J (2005) Analyzing and Filtering Surface-Wave Energy By Muting Shot Gathers. Journal of Environmental & Engineering Geophysics 10(3):307–322

Johnson D, Dudgeon D (1993) Array signal processing: Ptr prentice hall. Englewood Cliffs, N J p 533

Lawrence JF, Denolle M, Seats KJ, Prieto Ga (2013) A numeric evaluation of attenuation from ambient noise correlation functions. Journal of Geophysical Research: Solid Earth 118(12):6134–6145

Le Feuvre M, Joubert A, Leparoux D, Côte P (2015) Passive multi-channel analysis of surface waves with cross-correlations and beamforming. application to a sea dike. Journal of Applied Geophysics 114:36–51

Lepore S, Grad M (2020) Relation between ocean wave activity and wavefield of the ambient noise recorded in northern poland. Journal of Seismology 24(6):1075–1094

Li YE, Nilot E, Feng X (2020) Observation of guided and reflection p-waves in urban ambient noise cross-correlograms. In: SEG Technical Program Expanded Abstracts 2020, Society of Exploration Geophysicists, pp 2100–2104

Li Z, Lynn W, Chambers R, Larner K, Abma R (1991) Enhancements to prestack frequency-wavenumber (fk) migration. Geophysics 56(1):27–40

Lin FC, Moschetti MP, Ritzwoller MH (2008) Surface wave tomography of the western United States from ambient seismic noise: Rayleigh and Love wave phase velocity maps. Geophysical Journal International 173(1):281–298

Lin FC, Ritzwoller MH, Snieder R (2009) Eikonal tomography: surface wave tomography by phase front tracking across a regional broad-band seismic array. Geophysical Journal International 177(3):1091–1110

Liu Y, Xia J, Cheng F, Xi C, Shen C, Zhou C (2020) Pseudo-linear-array analysis of passive surface waves based on beamforming. Geophysical Journal International pp 640–650, DOI 10.1093/gji/ggaa024

Louie JN (2001) Faster, Better: Shear-Wave Velocity to 100 Meters Depth from Refraction Microtremor Arrays. Bulletin of the Seismological Society of America 91(2):347–364

Luo Y, Xia J, Miller RD, Xu Y, Liu J, Liu Q (2008) Rayleigh-Wave Dispersive Energy Imaging Using a High-Resolution Linear Radon Transform. Pure and Applied Geophysics 165(5):903–922, DOI 10.1007/s00024-008-0338-4

Maraschini M, Ernst F, Foti S, Socco LV (2010) A new misfit function for multimodal inversion of surface waves. Geophysics 75(4):G31–G43, DOI 10.1190/1.3436539

McMechan GA, Yedlin MJ (1981) Analysis of dispersive waves by wave field transformation. Geophysics 46(6):869–874

Mi B, Xia J, Shen C, Wang L (2018) Dispersion energy analysis of rayleigh and love waves in the presence of low-velocity layers in near-surface seismic surveys. Surveys in Geophysics 39(2):271–288

Mi B, Xia J, Bradford JH, Shen C (2020) Estimating near-surface shear-wave-velocity structures via multichannel analysis of rayleigh and love waves: An experiment at the boise hydrogeophysical research site. Surveys in Geophysics 41(2):323–341

Mikesell TD, Gribler G, Xu Z, Haney MM, et al. (2017) High-resolution dispersion images from deblurred masw. In: 2017 SEG International Exposition and Annual Meeting, Society of Exploration Geophysicists

Miller RD, Xia J, Park CB, Ivanov JM (1999) Multichannel analysis of surface waves to map bedrock. The Leading Edge 18(12):1392–1396

Nakahara H (2006) A systematic study of theoretical relations between spatial correlation and Green's function in one-, two- and three-dimensional random scalar wavefields. Geophysical Journal International 167(3):1097–1105, DOI 10.1111/j.1365-246X.2006.03170.x

Nakata N (2020) Pseudo arrivals generated by frequency normalization for seismic interferometry with scattered waves—stationary-phase analysis. In: SEG Technical Program Expanded Abstracts 2020, Society of Exploration Geophysicists, pp 2085–2089

Nakata N, Snieder R, Tsuji T, Larner K, Matsuoka T (2011) Shear wave imaging from traffic noise using seismic interferometry by cross-coherence. Geophysics 76(6):SA97–SA106

Nakata N, Chang JP, Lawrence JF, Boué P (2015) Body wave extraction and tomography at long beach, california, with ambient-noise interferometry. Journal of Geophysical Research: Solid Earth 120(2):1159–1173, DOI 10.1002/2015JB011870

Nakata N, Boué P, Brenguier F, Roux P, Ferrazzini V, Campillo M (2016) Body and surface wave reconstruction from seismic noise correlations between arrays at Piton de la Fournaise volcano. Geophysical Research Letters 43, DOI 10.1002/2015GL066997

Nazarian S, Stokoe II KH, Hudson WR (1983) Use of spectral analysis of surface waves method for determination of moduli and thicknesses of pavement systems. Transportation Research Record (930)

O'Connell DRH, Turner JP (2011) Interferometric Multichannel Analysis of Surface Waves (IMASW). Bulletin of the Seismological Society of America 101(5):2122–2141

Okada H, Suto K (2003) The microtremor survey method. Society of Exploration Geophysicists

Pan Y, Xia J, Xu Y, Gao L, Xu Z (2016a) Love-wave waveform inversion in time domain for shallow shear-wave velocity. Geophysics 81(1):R1–R14, DOI 10.1190/geo2014-0225.1

Pan Y, Xia J, Xu Y, Xu Z, Cheng F, Xu H, Gao L (2016b) Delineating Shallow S - Wave Velocity Structure Using Multiple Ambient-Noise Surface-Wave Methods: An Example from Western Junggar, China. Bulletin of the Seismological Society of America 106(2):327–336, DOI 10.1785/0120150014

Pan Y, Gao L, Bohlen T (2019) High-resolution characterization of near-surface structures by surface-wave inversions: From dispersion curve to full waveform. Surveys in Geophysics 40(2):167–195

Pang J, Cheng F, Shen C, Dai T, Ning L, Zhang K (2019) Automatic passive data selection in time domain for imaging near-surface surface waves. Journal of Applied Geophysics 162:108–117, DOI 10.1016/j.jappgeo.2018.12.018

Park C, Miller R, Laflen D, Neb C, Ivanov J, Bennett B, Huggins R (2004) Imaging dispersion curves of passive surface waves. In: SEG technical program expanded abstracts 2004, Society of Exploration Geophysicists, pp 1357–1360

Park CB, Carnevale M (2010) Optimum masw survey—revisit after a decade of use. In: GeoFlorida 2010: Advances in Analysis, Modeling & Design, pp 1303–1312

Park CB, Miller RD, Xia J (1998) Imaging dispersion curves of surface waves on multi-channel record. In: SEG Technical Program Expanded Abstracts 1998, Society of Exploration Geophysicists, pp 1377–1380

Park CB, Miller RD, Xia J (1999) Multichannel analysis of surface waves. Geophysics 64(3):800–808

Park CB, Miller RD, Ivanov J (2002) Filtering Surface Waves. In: Symposium on the Application of Geophysics to Engineering and Environmental Problems 2002, Environment and Engineering Geophysical Society, Figure 1, pp SEI9–SEI9, DOI 10.4133/1.2927182

Picozzi M, Parolai S, Bindi D (2010) Deblurring of frequency-wavenumber images from small-scale seismic arrays. Geophysical Journal International 181(1):357–368, DOI 10.1111/j.1365-246X.2009.04471.x

Poupinet G, Ellsworth W, Frechet J (1984) Monitoring velocity variations in the crust using earthquake doublets: An application to the calaveras fault, california. Journal of Geophysical Research: Solid Earth 89(B7):5719–5731

Prieto G, Lawrence J, Beroza G (2009) Anelastic earth structure from the coherency of the ambient seismic field. Journal of Geophysical Research: Solid Earth 114(B7)

Rafaely B, Weiss B, Bachmat E (2007) Spatial aliasing in spherical microphone arrays. IEEE Transactions on Signal Processing 55(3):1003–1010

Ren L, Gao F, Wu Y, Williamson P, Wang W, McMechan GA (2020) Automatic picking of multi-mode dispersion curves using cnn-based machine learning. In: SEG Technical Program Expanded Abstracts 2020, Society of Exploration Geophysicists, pp 1551–1555

Rost S, Thomas C (2002) Array seismology: Methods and applications. Reviews of Geophysics 40(3):1008, DOI 10.1029/2000RG000100

Safani J, O'Neill A, Matsuoka T, Sanada Y (2005) Applications of love wave dispersion for improved shear-wave velocity imaging. Environmental and Engineering Geophysics 10(2):135–150

Schwab F, Knopoff L (1972) Fast surface wave and free mode computations. In: Methods in Computational Physics: Advances in Research and Applications, vol 11, Elsevier, pp 87–180

Shapiro NM, Campillo M (2004) Emergence of broadband rayleigh waves from correlations of the ambient seismic noise. Geophysical Research Letters 31(7)

Snieder R (2004) Extracting the green's function from the correlation of coda waves: A derivation based on stationary phase. Physical Review E 69(4):046610

Snieder R, Miyazawa M, Slob E, Vasconcelos I, Wapenaar K (2009) A Comparison of Strategies for Seismic Interferometry. Surveys in Geophysics 30(4-5):503–523, DOI 10.1007/s10712-009-9069-z

Socco LV, Foti S, Boiero D (2010) Surface-wave analysis for building near-surface velocity models—established approaches and new perspectives. Geophysics 75(5):75A83–75A102

Song YY, Castagna JP, Black RA, Knapp RW (1989) Sensitivity of near-surface shear-wave velocity determination from rayleigh and love waves. In: SEG Technical Program Expanded Abstracts 1989, Society of Exploration Geophysicists, pp 509–512

Stokoe KI, Nazarian S (1983) Effectiveness of ground improvement from spectral analysis of surface waves. In: Proceeding of the eighth European conference on soil mechanics and foundation engineering

Strobbia C, Cassiani G (2011) Refraction microtremors: Data analysis and diagnostics of key hypotheses. Geophysics 76(3), DOI 10.1190/1.3560246

Thorson JR, Claerbout JF (1985) Velocity-stack and slant-stack stochastic inversion. Geophysics 50(12):2727–2741

Tromp J, Luo Y, Hanasoge S, Peter D (2010) Noise cross-correlation sensitivity kernels. Geophysical Journal International 183(2):791–819

Tsai VC, Moschetti MP (2010) An explicit relationship between time-domain noise correlation and spatial autocorrelation (SPAC) results. Geophysical Journal International 182(1):454–460, DOI 10.1111/j.1365-246X.2010.04633.x

Turner G (1990) Aliasing in the tau-p transform and the removal of spatially aliased coherent noise. Geophysics 55(11):1496–1503

Wapenaar K (2004) Retrieving the elastodynamic green's function of an arbitrary inhomogeneous medium by cross correlation. Physical Review Letters 93(25):254301

Wapenaar K, van der Neut J, Ruigrok E, van der Neut J (2008) Passive seismic interferometry by multidimensional deconvolution. Geophysics 73(NO.6):A51—-A56

Wathelet M, Jongmans D, Ohrnberger M (2004) Surface-wave inversion using a direct search algorithm and its application to ambient vibration measurements. Near Surface Geophysics 2(4):211–221

Winsborrow G, Huws D, Muyzert E (2003) Acquisition and inversion of love wave data to measure the lateral variability of geo-acoustic properties of marine sediments. Journal of Applied Geophysics 54(1-2):71–84

Xi C, Mi B, Dai T, Liu Y, Ning L (2020) Spurious signals attenuation using svd-based wiener filter for near-surface ambient noise surface wave imaging. Journal of Applied Geophysics 183:104220

Xi C, Xia J, Mi B, Dai T, Liu Y, Ning L (In Review) Modified frequency-bessel transform method for dispersion imaging of rayleigh waves from ambient seismic noise

Xia J, Miller RD, Park CB (1999) Estimation of near-surface shear-wave velocity by inversion of rayleigh waves. Geophysics 64(3):691–700

Xia J, Miller RD, Park CB, Ivanov J (2000) Construction of 2-d vertical shear-wave velocity field by the multichannel analysis of surface wave technique. In: 13th EEGS Symposium on the Application of Geophysics to Engineering and Environmental Problems, European Association of Geoscientists & Engineers, pp cp–200

Xia J, Miller RD, Park CB, Tian G (2003) Inversion of high frequency surface waves with fundamental and higher modes. Journal of Applied Geophysics 52(1):45–57

Xia J, Xu Y, Miller RD (2007) Generating an image of dispersive energy by frequency decomposition and slant stacking. Pure and Applied Geophysics 164(5):941–956

Xia J, Miller RD, Xu Y, Luo Y, Chen C, Liu J, Ivanov J, Zeng C (2009) High-frequency rayleigh-wave method. Journal of Earth Science 20(3):563–579

Xia J, Xu Y, Luo Y, Miller RD, Cakir R, Zeng C (2012) Advantages of Using Multichannel Analysis of Love Waves (MALW) to Estimate Near-Surface Shear-Wave Velocity. Surveys in Geophysics 33(5):841–860, DOI 10.1007/s10712-012-9174-2

Xu Y, Zhang B, Luo Y, Xia J (2013) Surface-wave observations after integrating active and passive source data. The Leading Edge 32(6):634–637

Xu Z, Xia J, Luo Y, Cheng F, Pan Y (2016) Potential misidentification of love-wave phase velocity based on three-component ambient seismic noise. Pure and Applied Geophysics 173(4):1115–1124

Xu Z, Dylan Mikesell T, Xia J, Cheng F (2017) A comprehensive comparison between the refraction microtremor and seismic interferometry methods for phase-velocity estimation. Geophysics 82(6):EN99–EN108

Yan FG, Cao B, Rong JJ, Shen Y, Jin M (2016) Spatial aliasing for efficient direction-of-arrival estimation based on steering vector reconstruction. EURASIP Journal on Advances in Signal Processing 2016(1):1–8

Yang Y, Ritzwoller MH, Levshin AL, Shapiro NM (2007) Ambient noise Rayleigh wave tomography across Europe. Geophysical Journal International 168(1):259–274

Yao H, van der Hilst RD (2009) Analysis of ambient noise energy distribution and phase velocity bias in ambient noise tomography, with application to SE Tibet. Geophysical Journal International 179(2):1113–1132

Yilmaz O (1987) Seismic data processing, society of exploration geophysicists, tulsa

Yin X, Xia J, Shen C, Xu H (2014) Comparative analysis on penetrating depth of high-frequency Rayleigh and Love waves. Journal of Applied Geophysics 111(0):86–94, DOI 10.1016/j.jappgeo.2014.09.022

Zeng C, Xia J, Liang Q, Chen C (2007) Comparative analysis on sensitivities of love and rayleigh waves. In: SEG Technical Program Expanded Abstracts 2007, Society of Exploration Geophysicists, pp 1138–1141

Zhan Z (2019) Distributed Acoustic Sensing Turns Fiber-Optic Cables into Sensitive Seismic Antennas. Seismological Research Letters DOI 10.1785/0220190112

Zhang K, Li H, Wang X, Wang K (2020) Retrieval of shallow s-wave profiles from seismic reflection surveying and traffic-induced noise. Geophysics 85(6):EN105–EN117

Zhou C, Xi C, Pang J, Liu Y (2018) Ambient noise data selection based on the asymmetry of cross-correlation functions for near surface applications. Journal of Applied Geophysics 159:803–813

Layer number	$\mathbf{V_p}(m/s)$	$\mathbf{V_s}(m/s)$	$\boldsymbol{\rho}(g/cm^3)$	$\mathbf{h}(m)$
1	400	800	2.0	10
2	200	400	2.0	10
3	600	1200	2.0	10
Half-space	800	1600	2.0	Infinite

Table 1 Parameters of a four-layer model.

Layer number	$\mathbf{V_p}(m/s)$	$\mathbf{V_s}(m/s)$	$\boldsymbol{\rho}(g/cm^3)$	$\mathbf{h}(m)$
1	200	800	2.0	10
Half-space	400	1200	2.0	Infinite

Table 2 Parameters of a two-layer model.

List of Tables

List of Figures

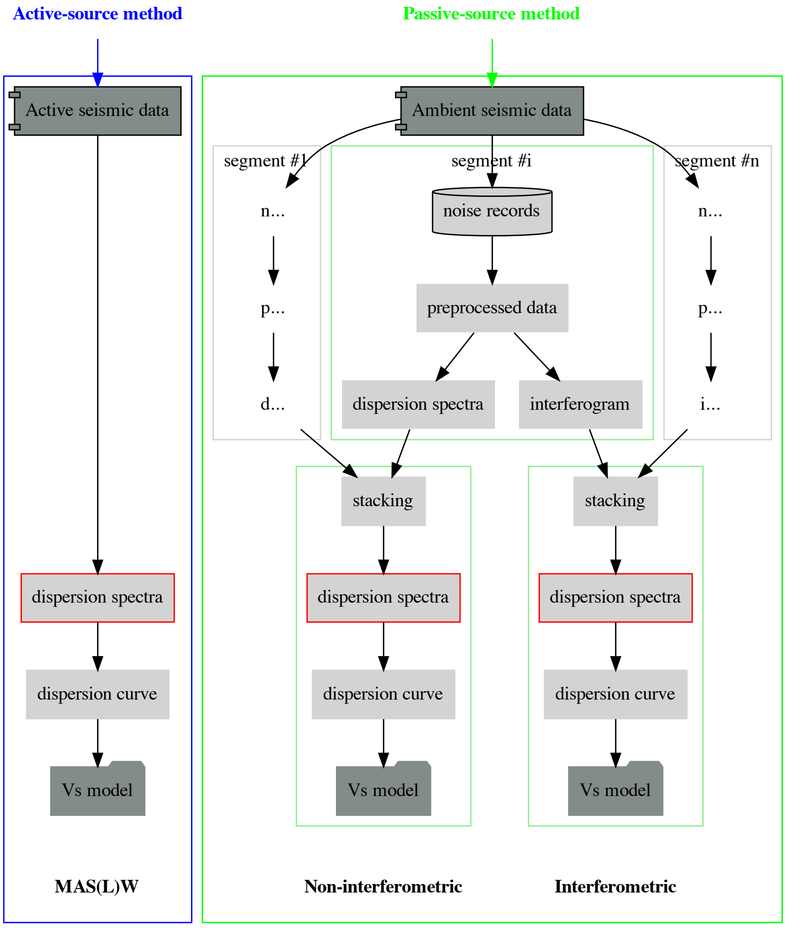

Fig. 1 Flowchart for two types of surface wave methods, the active-source method (the left panel) and the passive-source method (the right panel).

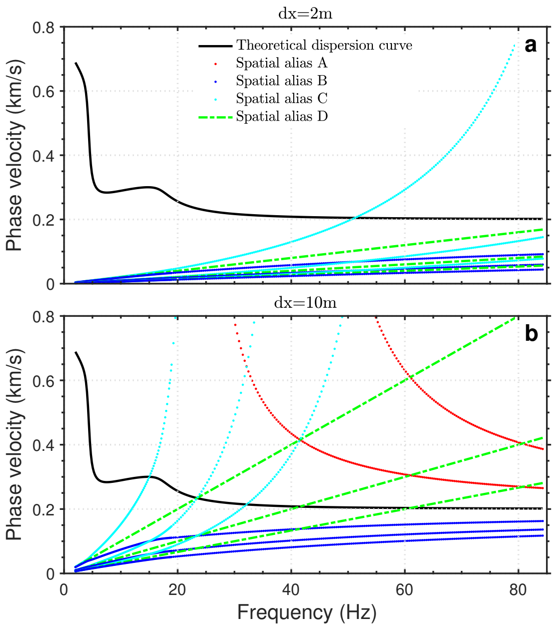

Fig. 2 A comparison of the predicted spatial aliasing with different spatial sampling, $dx = 2m$ (a) and $dx = 10m$ (b). The black curves show the theoretical dispersion curve; four colored, red, blue, cyan, green, dotted curves represent four types, A, B, C, D, spatial aliasing, respectively.

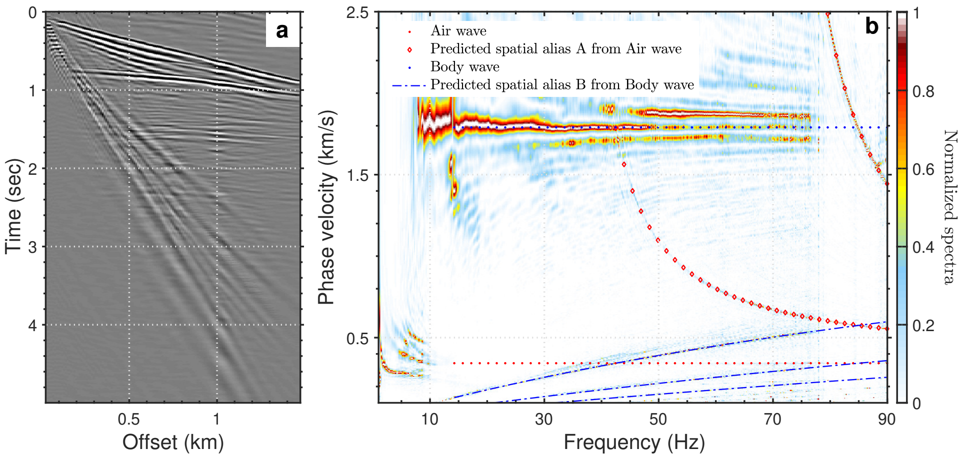

Fig. 3 An example of the type A and B spatial aliasing. a). the observed seismic shot gather; b). the obtained dispersion measurement. The red dotted line indicates the weak air wave energy; the red diamond curves represent the predicted type A spatial aliasing from air wave; the blue dotted line indicates the non-dispersive body wave energy; the blue dash-dot curves represent the predicted type B spatial aliasing.

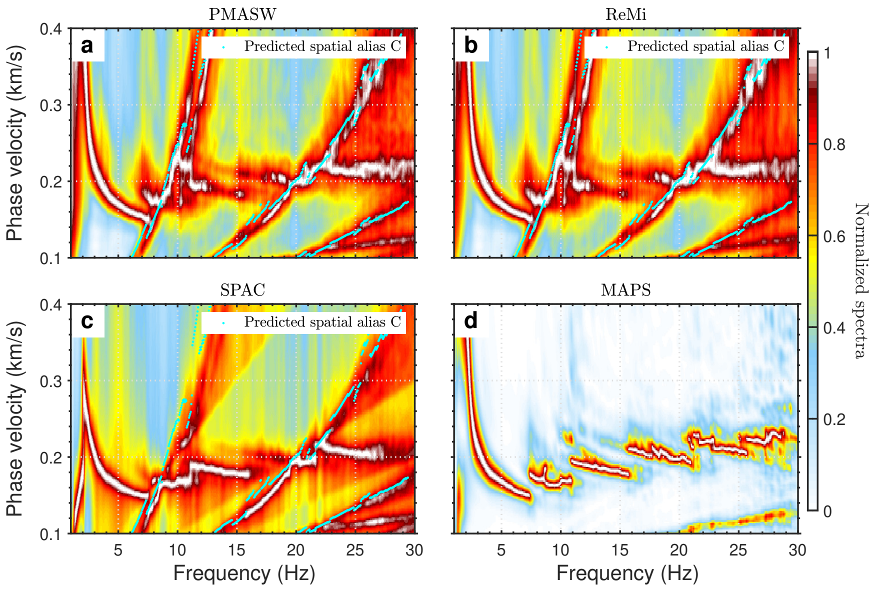

Fig. 4 An example of the type C spatial aliasing from Cheng et al. (2018b). a-d present the obtained dispersion spectra using different passive-source surface wave imaging methods, PMASW, ReMi, SPAC, and MAPS, respectively. The cyan dotted curves indicate the predicted type C spatial aliasing for each dispersion measurement.

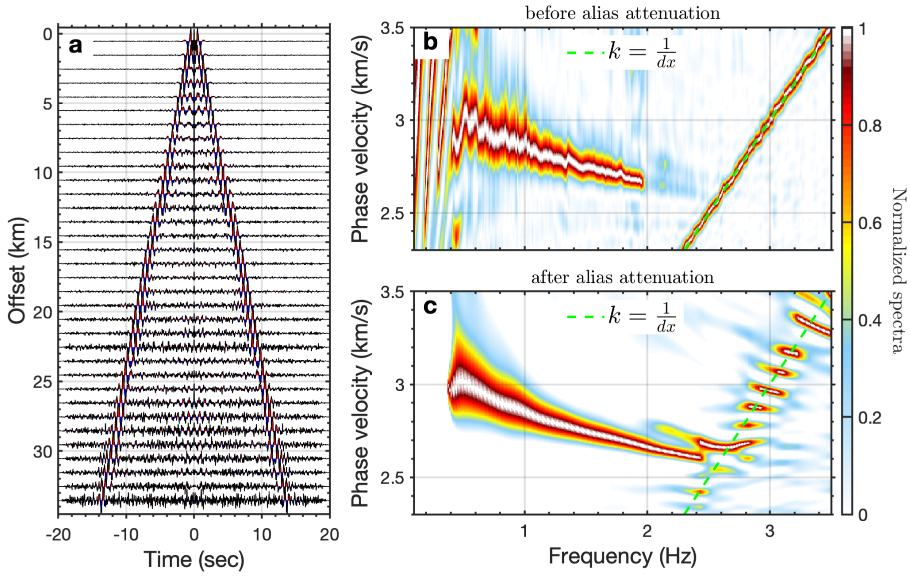

Fig. 5 An example of the type D spatial aliasing. a). the bin-stacked virtual source gather retrieved from ambient noise interferometry; b) and c). the obtained dispersion measurements before and after aliasing attenuated. The green dashed line indicates the predicted spatial aliasing. Note that the positive time lag and the negative time lag are averaged together during the bin-stacking.

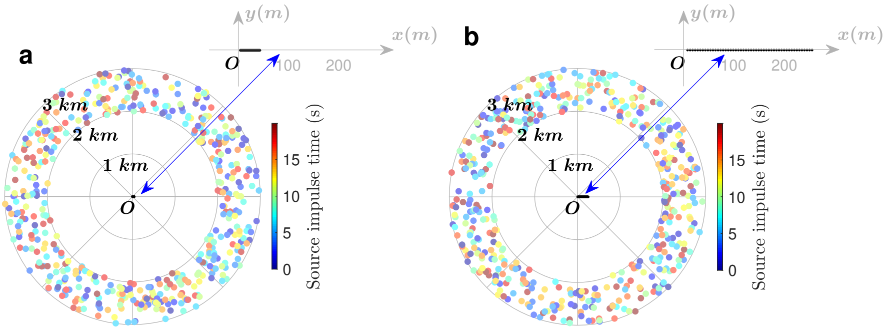

Fig. 6 Random noise sources and receivers configurations for seismic noise modeling with different array length, 50m (a) and 250m (b). The black dots denote the receivers; the random sources are color coded by the random source impulse time.

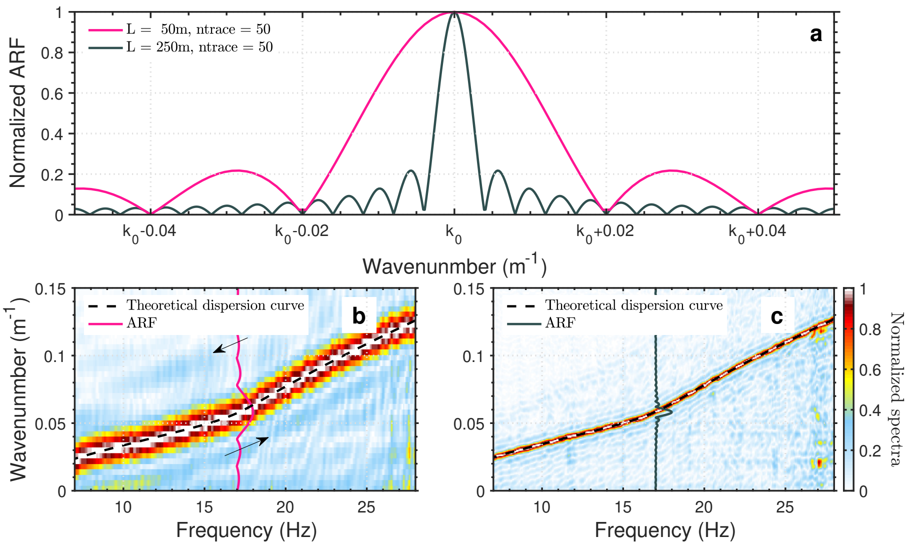

Fig. 7 a) Array response functions for two linear arrays with different array lengths, 50m (the pink line) and 250m (the gray line). b-c present the corresponding dispersion spectra for two linear arrays, respectively. The black dashed lines in b and c are the theoretical dispersion curves; two colored, pink and gray, solid lines are the corresponding ARFs at frequency 17 Hz; the black arrows on b indicate the wiggles artifacts from the array response.

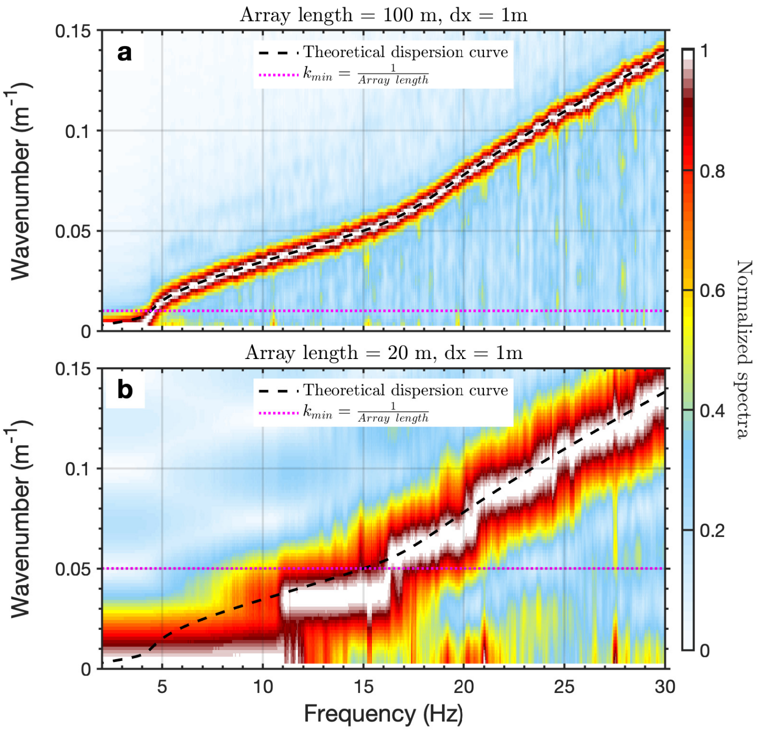

Fig. 8 Effects of different array lengths, 100m (a) and 20m (b), on the minimum wavenumber (or the maximum wavelength) for the surface wave dispersion measurement. The pink dashed lines indicate the minimum wavenumber (or the maximum wavelength) inferred from the array length; the black dashed lines represent the theoretical dispersion curve. Note that no data preprocessing procedure is included prior to noise cross-correlation.

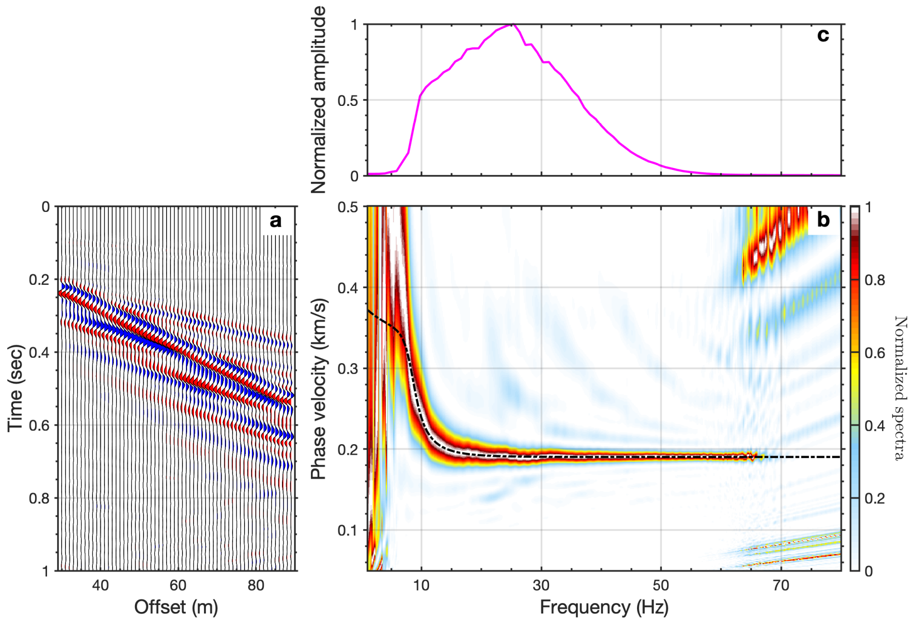

Fig. 9 a). A synthetic active-source surface wave shot gather; b). the obtained dispersion spectra using the phase-shift method; c). the normalized spectrum. The black dashed line on b represents the theoretical dispersion curve.

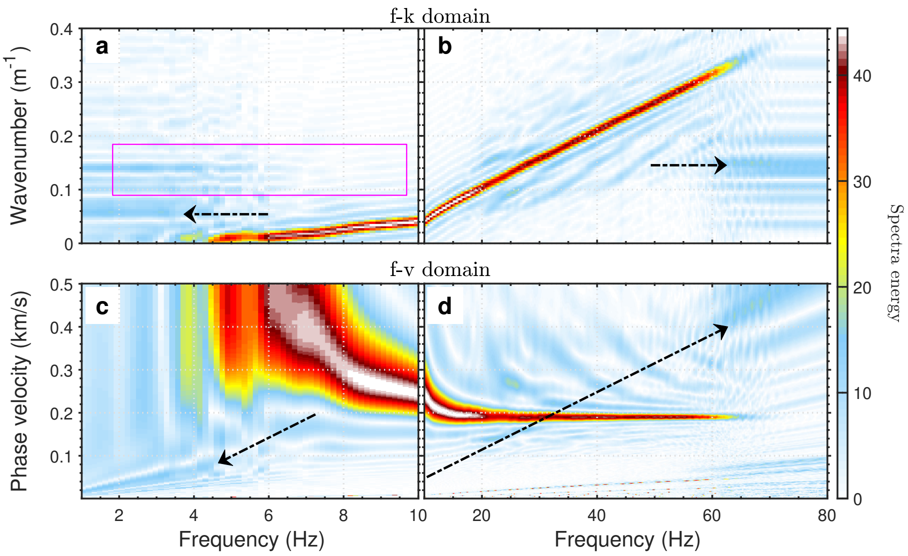

Fig. 10 a-b present the obtained dispersion spectra without frequency-direction normalization in $f-k$ domain; c-d present the obtained dispersion spectra without frequency-direction normalization in $f-v$ domain. The black dashed arrows on a and b indicate the horizontal artifacts with constant wavenumber; the black dashed arrows on c and d indicate the radial pattern artifacts; the pink box highlights the consistency between the horizontal artifacts at lower frequency (< 5Hz) and wiggles artifacts from the array response artifacts at the higher frequency (> 6Hz).

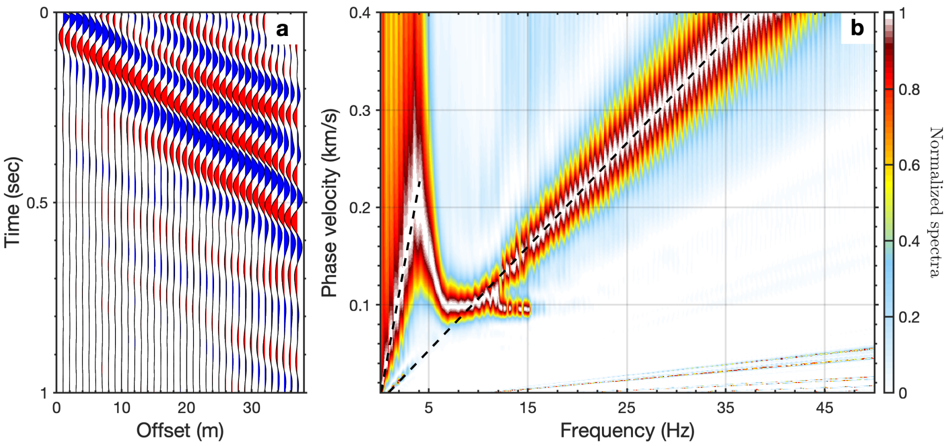

Fig. 11 An example of the radial pattern artifacts for field example #1. a). The bin-stacked virtual source gather retrieved from ambient noise interferometry without noise data preprocessing. The bin-size is 1m. b). Dispersion measurement with distinct artifacts. The black dashed lines highlight the radial pattern artifacts.

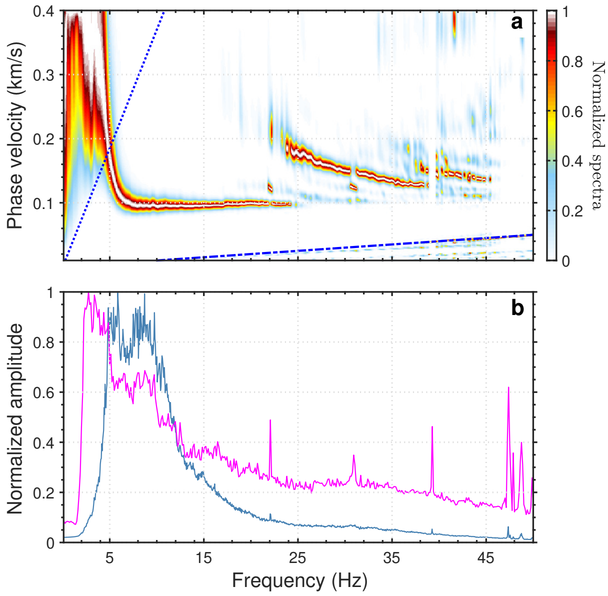

Fig. 12 a). Dispersion spectra with spectral whitening included prior to cross-correlation. The blue dotted line indicates the minimum wavenumber (or the maximum wavelength) inferred from the array length; the blue dashed line indicates the maximum wavenumber (or the minimum wavelength) inferred from two times of the Nyquist wavenumber ($k_{max} = 2 * \frac{1}{2*dx}$). b). The spectrum of extracted cross-correlations without (the dark blue curve) and with (the pink curve) spectral whitening.

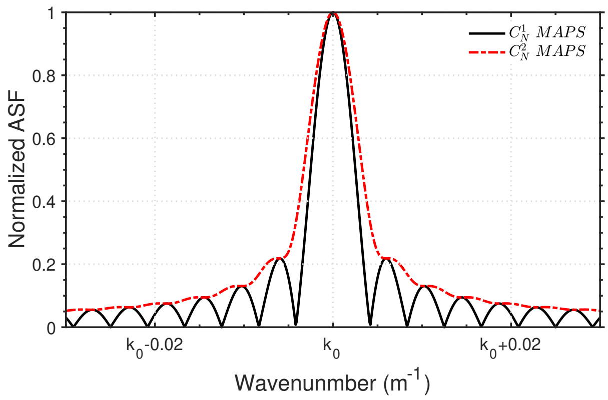

Fig. 13 A comparison of ARFs between one virtual-source gather and multiple virtual-sources gather. Here we take an array of 24 sensors with 10m spatial interval as example.

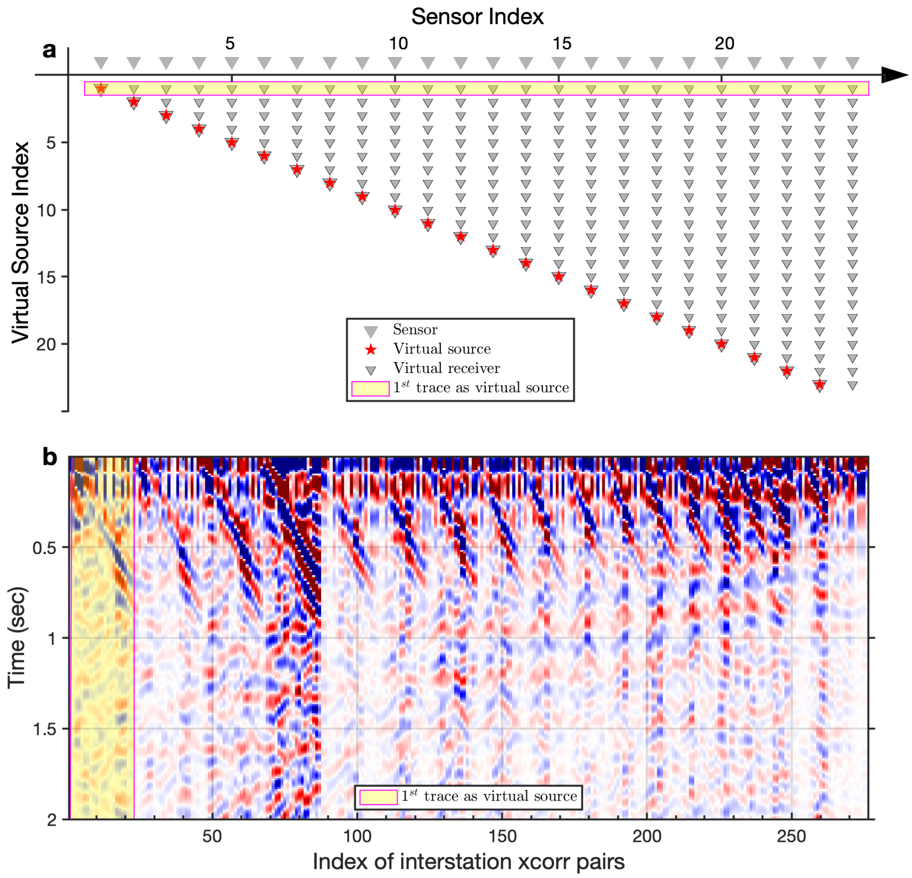

Fig. 14 a). Virtual source and virtual receiver configuration for C_N^2 inter-station cross-correlation pairs. b). The extracted C_N^2 inter-station cross-correlation pairs using ambient noise interferometry. The yellow box highlights the one virtual-source gather with the first trace as the virtual source.

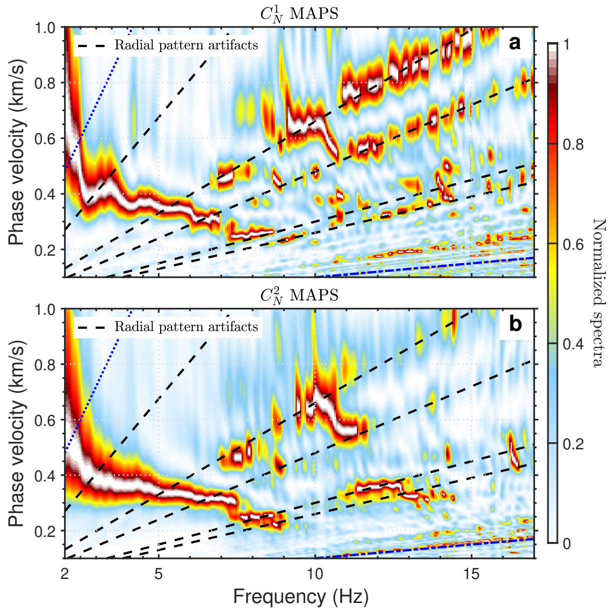

Fig. 15 a). Dispersion spectra from the one virtual-source gather by using MAPS. b). Dispersion spectra from the multiple virtual-sources gather by using MAPS. The black dashed lines indicate the radial pattern artifacts.

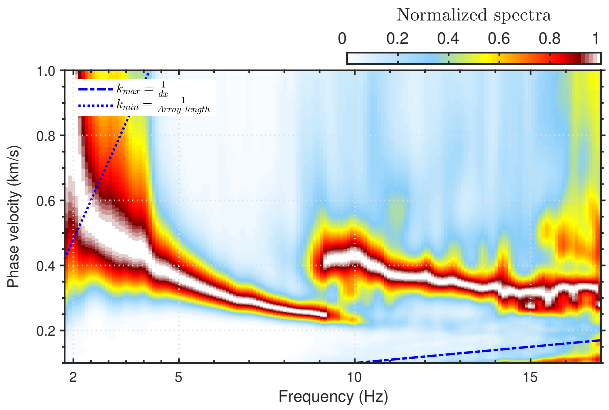

Fig. 16 An example of the radial pattern artifacts attenuation using data selection technique from Cheng et al. (2019).

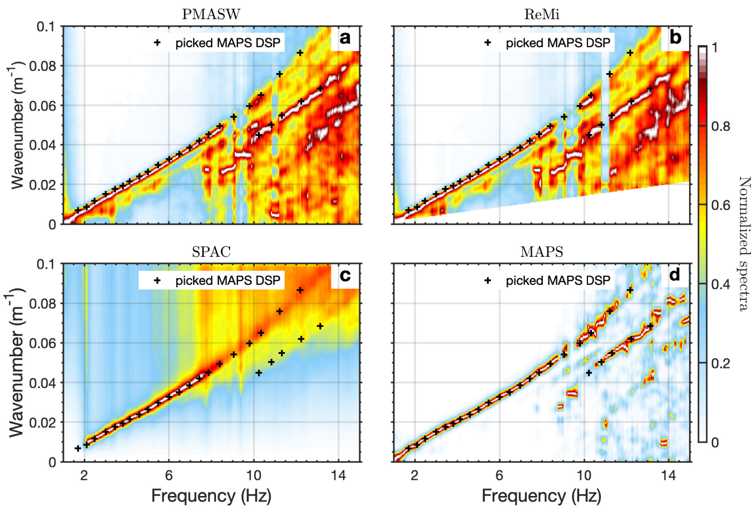

Fig. 17 An example of the artifacts from the non-interferometric methods from Cheng et al. (In reviewb). a-d present the obtained dispersion spectra using different passive-source surface wave imaging methods, PMASW, ReMi, SPAC, and MAPS, respectively.

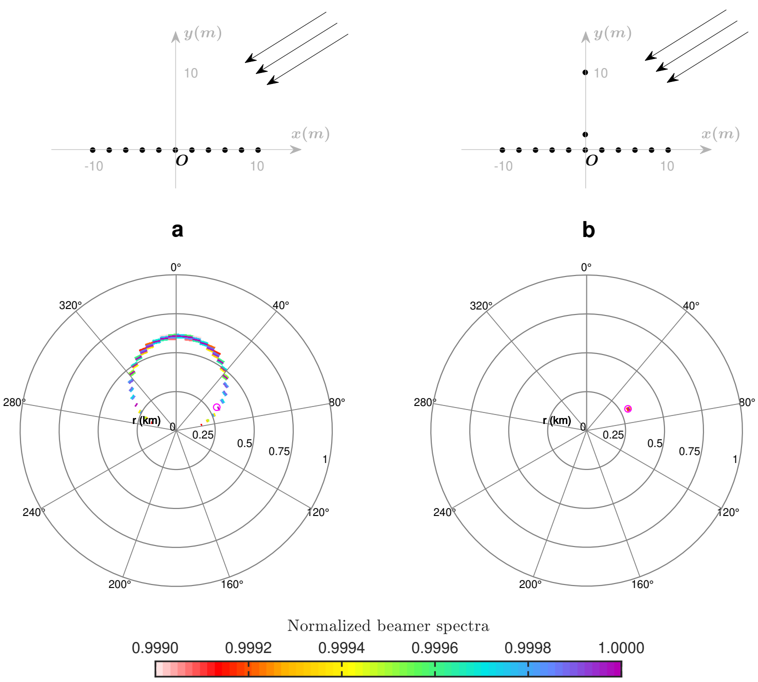

Fig. 18 Array responses for the linear array (a) and the pseudo-linear array (b). The black dots denote the receivers; the black arrows indicate the plane wave.